Czech University of Life Sciences Prague
Faculty of Environmental Sciences

Czech University of Life Sciences Prague
Faculty of Environmental Sciences

Surface Urban Heat Island in Prague: Retrospective Analysis, Heat-Related Mortality Links, and COVID-19 Lockdown Effect

Ing. Tugba Dogan

This dissertation thesis is submitted for the degree *Doctor of Philosophy* at the Department of Water Resources and Environmental Modeling.

Prague March 2024

Dissertation Thesis

Surface Urban Heat Island in Prague: Retrospective Analysis, Heat-Related Mortality Links, and COVID-19 Lockdown Effect

Author: Ing. Tugba Dogan

Supervisor: Mgr. Aleš Urban Ph.D.

Co-supervisor: prof. Ing. Martin Hanel, Ph.D.

I hereby declare that the dissertation thesis entitled *"Surface Urban Heat Island in Prague: Retrospective Analysis, Heat-Related Mortality Links, and COVID-19 Lockdown Effect"* submitted for the degree Doctor of Philosophy in Environmental Modelling field is my original work guided by my supervisor and my co-supervisor. Any information made by others or literal quotations are referenced. The thesis has not been published elsewhere.

....

Ing. Tugba Dogan

Acknowledgement

Abstract

In the face of escalating climate change, the frequency and intensity of heatwaves are projected to rise. Concurrently, the urban heat island effect exacerbates the adverse impacts of heatwaves, leading to an increase in heat-related mortality. To effectively address these mounting challenges, it is imperative to gain a comprehensive understanding of the effects of environmental changes on urban heat islands and their implications for public health. This study aims to provide a holistic assessment of the multifaceted impacts of urbanization on urban heat islands and establish a correlation with heat-related mortality during heat waves. This is achieved through three interconnected case studies, each with a distinct focus: the temporal evolution of Surface Urban Heat Island (SUHI) due to land cover change, the impacts of reduced emissions during the COVID-19 lockdown on atmospheric and surface Urban Heat Islands (UHIs), and the spatio-temporal relationships between SUHI intensity and heat-related mortality in Prague, Czechia. The first case study leverages CORINE Land Cover products and Landsat satellite images from five pivotal periods (1990, 2000, 2006, 2012, and 2018) to evaluate the effects of land cover change on SUHI. The second case study assesses the impact of the COVID-19 lockdown on UHI dynamics by comparing satellite images and weather station data from the lockdown period in March–April 2020 with a reference period in March–April 2017–2019. Daily MODIS images are used to examine changes in mean SUHI, while air temperature data from Prague weather stations are employed to analyze atmospheric UHI. The final case study explores the links between spatial distribution LST and heat-related mortality during heat waves using daily MODIS land surface temperature images and daily all-cause mortality data in ten Prague districts. Distributed lag non-linear models, adjusted for long-term trends

and seasonal cycles, are used to establish heat-related mortality risk of major heatwaves in Prague between 2001 and 2020. In conclusion, this thesis provides a comprehensive exploration of the complex interplay between urbanization, urban heat islands, and heat-related mortality. It underscores the importance of understanding these dynamics to develop effective strategies to mitigate the impacts of heatwaves, enhance urban resilience, and promote public health.

Contents

Part I

Introduction

Chapter I

Introduction

1.1   Urban Heat Island

Urban heat Island (UHI) phenomenon is defined as noticeably high temperature within the urban region compared to the surrounding rural vicinity (Figure 1.2) (Oke, 1973). Urban heat Island was introduced by Lake Howard who investigated UHI in London (Yang, Qian, Song and Zheng, 2016). Following studies of this concept were made for Paris and Vienna by Emilian Renou and Wilhelm Schemidt in the 19th and 20th centuries (Gartland, 2011). These temperature differences between urban and rural regions can be 10 to 15° C during the day and 5 to 10°C during night (Hashem Akbari et al., 2013). Figure 1.1 illustrates the cross-section of surface and air temperatures for daytime and nighttime throughout rural, suburban and urban areas.

Even though UHI effect occurs throughout all the seasons of the year, its existence during the summer in warm climate cities is a matter of immense public policy concern due to increasing exposure of high summer temperatures which precipitates a rise in air conditioning demand, an increase in air pollution, and a spike in heat- stress related mortality and illness.
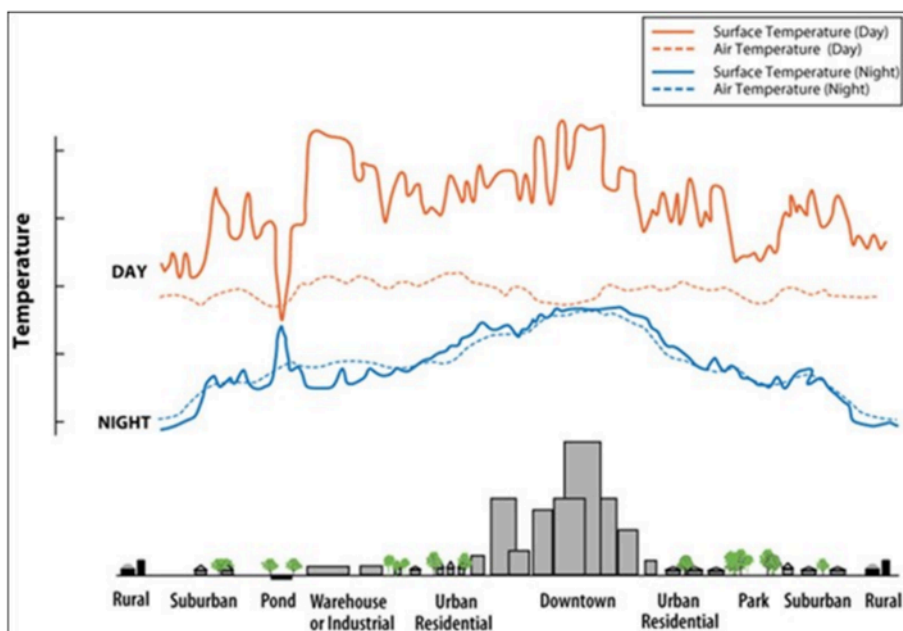
Figure 1.1. Temperature profile for urban, suburban and rural areas during day and night (EPA, 2018).

UHI was categorized into three parts related to the altitude at which they are measured; boundary layer heat island, canopy layer heat island, and surface urban heat island (Figure 1.2.) (Oke, 1976; Zhang, Zhong, Feng and Wang, 2009). The boundary layer urban heat island (BLUHI) measures temperature differences one to two kilometers above roof-height at altitudes and affects meso-scale (Menut, Flamant, Pelon and Flamant, 1999). The canopy layer urban heat island (CLUHI) atmospheric boundary layer ranging from the land surface to roof-top level. Thermal radiation and warm air rising from the UCL causes warming in the UBL (Oke, 1987).

Acquisition of the temperature is different for these three categories since their altitude and scale vary. Microwave radiometers for BLUHI, networks of meteorological sensors data CLUHI and remote sensing data for the surface urban heat island (SUHI) which represents surface temperature (Oke, 1976; Voogt, 2007). Thermal remote sensing – uses

non-contact instruments that sense longwave or thermal infrared radiation to estimate surface temperature. Due to freely available satellite images and its capability of showing spatial patterns of the city, it has increasing popularity in urban climate studies.
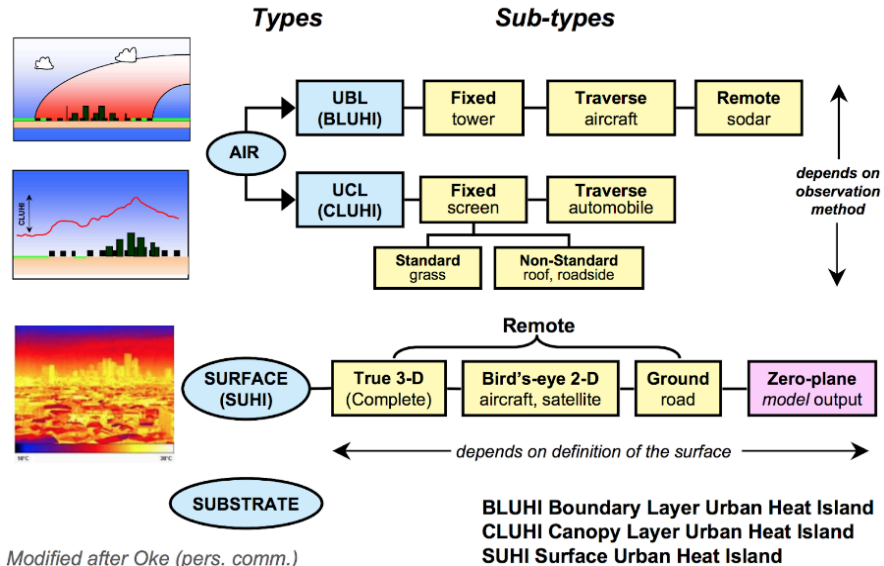
Figure 1.2. UHI Types and Measurement Approaches (Voogt, 2007).

1.2 Causes of Urban Heat Island

Oke (1982) assembled and summarized causes of the UHI as follows:
- accelerated absorption of short-wave radiation due to multiple reflection; anthropogenic heat resources;
- decreased outgoing long wave radiation because of reduced sky view (air pollutants);
- decreased radiative cooling;
- increased sensible heat storage due to higher thermal admittance of constructing substances;

- decreased evapotranspiration due to construction material;
- decreased total turbulent heat fluxes from wind speed reduction in the urban environment (Watson, 2012).
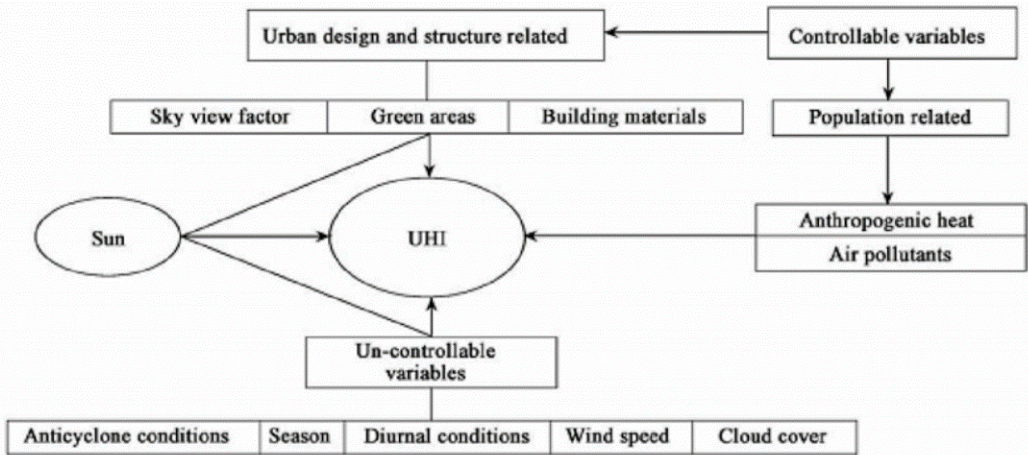
Figure 1.3. Causes of urban heat island (Rizwan, Dennis and Liu, 2008).

According to previous research (Rizwan, Dennis, and Liu, 2008) causes of UHI are categorized into two types: controllable and uncontrollable (Figure 1.3). This means that some factors contributing to UHI can be managed or mitigated through human intervention (controllable), while others are beyond human control (uncontrollable). Controllable factors are induced by population growth thus we can also name them human caused factors. They can be further divided into population related factors (such as anthropogenic heat and air pollutants) and urban design related factors (such as sky view factor, green areas, building materials) (Kei Wang Cheung, 2011). Major cause of urban heat island effect is urbanization which is the consequence of increasing population in the city.

Therefore, due to urbanization natural land cover is replaced by artificial urban surface. As a result, these altered natural surfaces are causing corruption in natural ecosystem services which affects evaporation, runoff water, air filtration, shade and wind patterns in the city. Moreover, built

up areas absorb solar radiation (shortwave and longwave radiation), block wind and trap heat inside the city. Weather parameters such as cloud cover, wind speed, diurnal situations, seasons and anticyclonic conditions, are taken into consideration as an uncontrolled element.
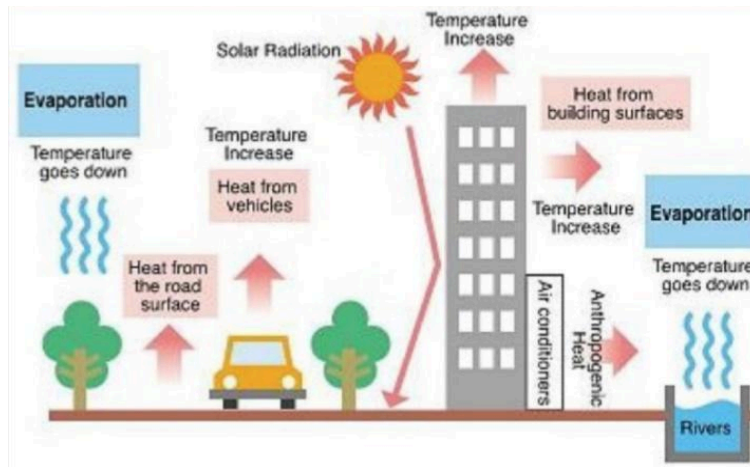
Figure 1.4. Causes of urban heat island (Urban Heat Islands, 2018).

Crucial anthropogenic heat resources that exaggerate UHI are fossil fuel usage for automobiles and heating/cooling of constructed infrastructure (Sailor and Lu, 2004). Furthermore, because of anthropogenic reasons, the increase of temperature is related to the function of shape insulation (Arnfield, 2003). Anthropogenic factor consequences on UHI also rely on the size, population and climate conditions of the region so it has a less impact on small cities than a city (Oke, 1982).

Size, form, composition, and neighborhood planning have an effect on the UHI (Chen et al., 2006). The reduction in air circulation and the overall decrease in the temperature within cities are predominantly due to high-rise buildings and cramped streets, which trap heat collected throughout the day (Bokaie et al., 2016).

1.3. Impacts of Urban Heat Island

UHIs have a significant impact on both human health and the environment. On one hand, they can lead to a range of health issues including general discomfort, heat stroke, sunburn, dehydration, and respiratory problems (Aguiar, 2012; EPA, 2016). On the other hand, they contribute to environmental changes such as the initiation of storms and precipitation (Dixon and Mote 2003), deterioration of air and water quality, and an increase in smog and humidity.

A study showed that temperature of rainwater increases from 21°C to 35°C after passing over pavements (Deilami, 2018). This rainwater may later flow into rivers and streams, which can have harmful effects on fauna in rivers and oceans (EPA, 2016). Moreover, inhabitants' need for cooler places in urban areas leads to an increase in energy demand, especially during summer (Magli et al., 2015). This increase results in the emission of greenhouse gasses and other air pollutants by electrical companies. This is caused by using fossil fuels by electrical plants to meet the extra demands of their clients (EPA, 2016).

Heat stroke, heat cramps, dehydration, and heat-related death are all an acute issue resulting from heat stress. During the 2003 Heat Wave, studies estimated about 15000 excess deaths in France, and up to 70000 deaths in whole Europe (Fouillet et al., 2006). In 1995 more than 739 people perished due to a heat wave in Chicago (Whitman et al., 1997). Cases of Heat Stroke skyrocket, as there is a demonstrable negative impact on the overall well being of the population during heatwaves (Argaud et al., 2007).

In addition to the health and environmental impacts, Urban Heat Islands (UHIs) also exert various negative influences on a city's economy. The increased health risks associated with UHIs can lead to higher medical expenses for individuals and communities. Furthermore, the ecological

changes triggered by UHIs can disrupt ecological services, potentially leading to increased costs for environmental management and restoration. Lastly, UHIs can result in excess energy usage, particularly for cooling during hot periods, which can significantly increase energy costs.

Therefore, it is crucial to develop effective strategies to mitigate the impacts of UHIs, considering their far-reaching implications for public health, environmental sustainability and sustainable urban planning. In order to combat these negative impacts, mitigation measures should be implemented into the city. Mitigation measures are created based on controllable factors of urban heat island effect in that city. Figure 1.5 shows essential mitigation measures for the cities which aims to reduce urban heat island effect.
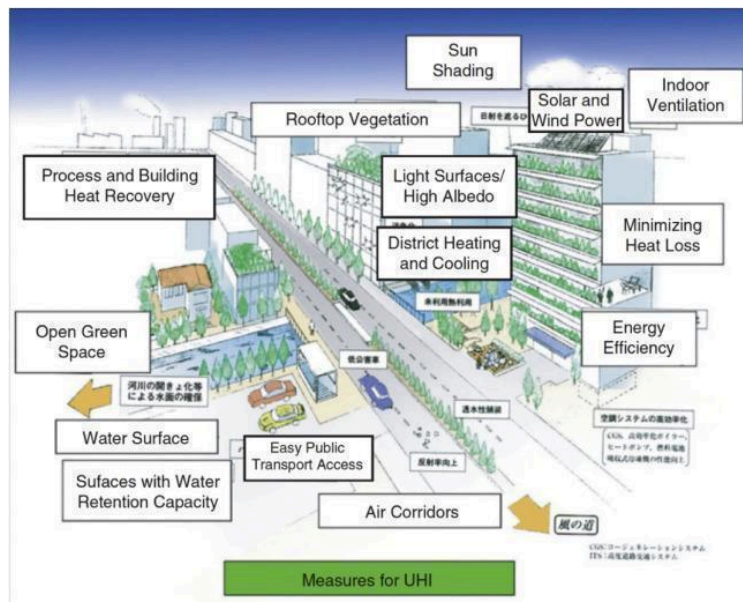
Figure 1.5. Mitigation Measures for the Urban Heat Island (Ichinose et al., 2008).

1.4. Remote sensing and SUHI

Remote sensing is used to estimate LST, which is a key parameter in SUHI studies. Satellites with thermal infrared sensors can capture thermal infrared radiation emitted by the Earth's surface, which is used to calculate LST. Thermal satellite remote sensing of LST provides high temporal resolution for monitoring SUHIs and enables analysis of the diurnal cycle of SUHI (Zakšek and Oštir, 2012). The list of satellites with thermal infrared sensors are shown in Figure 1.6 (Waver et al., 2016). Landsat and MODIS are most commonly used in SUHI studies.

Satellite	Sensor	Spectral resolution Number of TIR bands, wavelengths	Spatial resolution [m]	Temporal resolution [days]
Terra	ASTER	5 (8.5–11.6 μm)	90	16 on demand
Terra, Aqua	MODIS	16 (3.7–14.4 μm)	1000	2 (day and night) automatic
Landsat 8	TIRS	1 (10.3–12.5 μm)	100	16 automatic
Landsat 7	ETM+	1 (10.4–12.2 μm)	60 (od 31.05.2013 partially corrupted – 22% of a scene)	
NOAA	AVHRR/3	2/3 (3.5–12.5 μm)	4000	2 (day and night)
ENVISAT	AATSR	3 (3.7–12 μm)	1000	2 (day and night)
Meteosat 8, 9, 10	SEVIRI	8 (3.5–14.4 μm)	3000	0.01

Figure 1.6. The list of satellites with thermal infrared sensors (Waver et al., 2016).

1.5. Thesis Structure

The thesis consists of three case studies and is divided into two parts and five chapters. The **Part I** contains an introduction to urban heat island. The **Part II** consists of individual case studies:

- **Case Study I:** Evaluating the effects of land cover change on the change of surface urban heat island.

- **Case Study II:** Effect of COVID-19 Lockdown on Urban Heat Island Dynamics in Prague, Czechia.

- **Case Study III:** Links between the spatial distribution of the land surface temperature and heat-related mortality in Prague, Czech Republic.

Part II

Case Studies

Chapter II

Case Study I: Evaluating the effects of land cover change on the change of surface urban heat island

Abstract

The aim of this study is to evaluate the effects of land cover change on the change of surface urban heat island in the past 28 years in five different periods; 1990, 2000, 2006, 2012 and 2018 in Prague. For this purpose Landsat CORINE Land Cover status and change layer products, and Landsat 5 TM, Landsat ETM+, Landsat TIR/OLI satellite images were used. The UHI effects evaluation and its relationship with land cover change was analyzed qualitatively using Jenk's classification and quantitatively using SUHI indices. The results showed that the dominant land cover changes are from rural area to urban fabric in hinterland, mainly between 9-12 km distance from city center. This peri-urbanization is correlated with an increase in SUHI which have been steadily increasing since 2006. Land cover changes and SUHI class change comparison shows that land cover changes effects on SUHI varies depending on the location. Overall, these findings suggest that in order to mitigate the adverse effect of UHI effectively, urban planners and decision makers should consider the effect of land cover changes along with other factors affecting UHI.

2.1 Introduction

Cities contribute to climate change through high energy consumption and greenhouse gas emissions. Concurrently, they are also more susceptible to the adverse effects of climate change. These effects not only impact ecosystems but also pose a threat to human health and comfort, especially during extreme temperatures in the summer months. In addition to the challenge of climate change, cities experience the urban climate phenomenon known as the Urban Heat Island (UHI) effect. The UHI phenomenon is characterized by significantly higher temperatures within urban regions compared to surrounding rural areas (Oke, 1973).

The concept of the Urban Heat Island was first introduced by Luke Howard, who conducted a study on UHI in London (Yang, Qian, Song and Zheng, 2016). The primary cause of the UHI effect is urbanization, which leads to the replacement of natural land cover with artificial urban surfaces. This alteration disrupts natural ecosystem services, affecting evaporative cooling, runoff water, air filtration, shade, and wind patterns within the city. Furthermore, built-up areas absorb solar radiation (both shortwave and longwave), block wind, and trap heat within the urban canyon.

UHIs significantly affect human health and well-being such as; general discomfort, heatstroke, sunburn, dehydration and respiratory problems (Aguiar, 2012; EPA, 2016). Related to environmental effects, UHI contributes to the initiation of storms/precipitation (Dixon and Mote, 2003), a worsening of air and water quality, increasing smog and humidity. In order to combat all of these negative impacts, mitigation measures should be implemented into the city.

UHI was categorized into 3 parts related to the altitude at which they are measured; boundary layer heat island, canopy layer heat island, and

surface urban heat island (Oke, 1976; Zhang, Zhong, Feng and Wang, 2009). The boundary layer urban heat island (BLUHI) measures temperature differences one to two kilometers above roof-height at altitudes and affects meso-scale (Menut, Flamant, Pelon and Flamant, 1999). The canopy layer urban heat island (CLUHI) atmospheric boundary layer ranging from the land surface to rooftop level. Surface urban heat island (SUHI), land surface temperature (LST) is measured by thermal infrared sensors and satellite images.

One of the challenges for UHI studies is the limited number of meteorological stations, which makes it impossible to analyze spatial disturbed within the city due to its lack of spatial coverage. Thus, studies which use meteorological data can only analyze the difference between urban and rural stations. However, it still has limitations, due to elevation difference between stations, surrounding areas, land cover and openness of the station in terms of constant wind direction. On the contrary, with the remote sensing data it is possible to cover all the urban areas. With evolution and improvement of remote sensing techniques, analyzing UHI from satellite images up to 30 m horizontal resolution is achievable. For instance, Landsat thermal infrared bands have been utilized in several researches for urban heat island analyzes. According to a historical review related to surface urban heat island studies using satellite images, 53 % studies have used Landsat images (Zhou et al., 2018).

Many researches have demonstrated a correlation between urban heat island and urbanization. However, due to differences between image classification methods and accuracy, most studies are not comparable. In order to deal with this issue, researchers proposed LCZ local climate zones to classify images based on the thermal properties (Stewart and Oke, 2012). Although this is a significant advancement for SUHI research, since researchers use different data to create LCZs and accuracies are varied, their comparability is still a challenge. The most common approach for image classification is using the same image as LST retrieval. However, in the case of using several images to represent a period, which image should be selected is questionable. Another way to deal with this issue is using a common land cover data as CORINE Land Cover initiated by the European Environment Agency. This land cover data was used by

several researchers to analyze the relationship between land cover and SUHI, and found that urbanization caused increase in SUHI (Stathopoulou and Cartalis, 2007; Majkowska, Kolendowicz, Półrolniczak, Hauke and Czernecki, 2016 ; Lin, Jim, Deng and Wang, 2018).

The aims of this case study are as follows: (1) to analyze the spatiotemporal changes in land cover using CORINE land cover map in the years 1990, 2000, 2006 ,2012, 2018; (2) to derive land surface temperature from Landsat time series (Landsat 5 ™, Landsat ETM+, Landsat TIR/OLI); (3) to investigate the spatiotemporal distributions and relationships between land cover and UHI throughout the study period; (4) to examine the effects of land cover change on the change of urban heat island. The study area, Prague covers an area of 49.613 hectares with 1.301.135 inhabitants, as the most populated city of Czechia ("Statistics VDB", 2019). Due to its low elevation, especially in the city center, the city is vulnerable to UHI effect.

2.1 Methods

Following softwares has been used in this study; ArcGIS 10.5.1 (ESRI) for geospatial analysis; ENVI software was used for image pre-processing and retrieval of LST and R studio is used for raster analysis. A vector file which contains the administrative border of Prague was used to delineate the study area for CORINE and Landsat data.

2.1.1 Analyzing land cover changes from CORINE

To analyze land cover changes, the CORINE land cover data, downloaded from Copernicus Land Monitoring Service's website, was used (CORINE Land Cover, 2023).

The CORINE Land Cover (CLC) data for the periods 1990, 2000, 2006, 2012 and 2018 were chosen for land cover analysis. The CLC data have 44 land cover classes, however these classes were reclassified for this study based on their thermal similarities (see Table 2.1).

In order to demonstrate the distribution of land cover, land cover fractions relationship with distance from the urban center was analyzed by using the schema in Figure 2.1.

Table 2.1. Reclassified CORINE land cover classes used for the study.

| CORINE Land Cover Classes		Reclassified Classes
Level I	**Level II**	
1 Artificial Surfaces	11 Urban fabric	11
	12 Industrial, commercial and transport units	12
	13 Mine, dump and construction site	13
	14 Artificial, non-agricultural vegetated areas	14
2 Agricultural Areas	21 Arable land	20
	22 Permanent crops	
	23 Pastures	
	24 Heterogeneous agricultural areas	
3 Forest and Seminatural Areas	31 Forests	30
	32 Shrub and/or herbaceous vegetation associations	
	33 Open spaces with little or no vegetation	
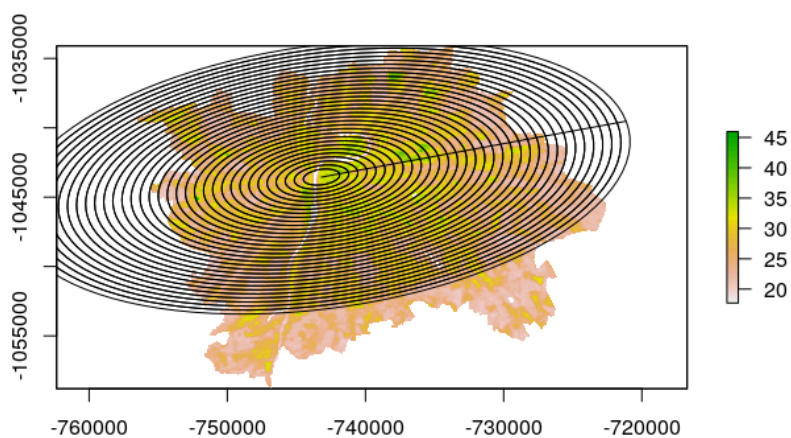
Figure 2.1. Land cover fractions against distance from the urban center accumulation of all periods.

2.1.2 Retrieving of LST from Landsat

In this study, Landsat 5 ™, Landsat ETM+, and Landsat TIR/OLI satellite images were obtained from the earth explorer website. (https://earthexplorer.usgs.gov/).

Because the UHI effect is more developed during the summer season, images were chosen between June to September. The study period is the same as CORINE land cover data (1990, 2000, 2006, 2012, 2018) and for each period one consecutive years are included so for each period three, in total fifteen remotely sensed images were used. The images selection criteria was the hottest and cloudless days in the summer season (less than 3% of the study area). A list of input Landsat images and acquisition times are provided in Appendix A (Table A1).

In order to retrieve LST, the Image Based method (IBM) based on the Landsat user's book, was used (Lin, Jim, Deng and Wang, 2018; Landsat 8 users' book, 2019).

Prior to LST calculation, clouds and cloud shadows which have a direct effect on land surface temperature, were masked using Landsat quality bands (Avdan and Jovanovska, 2016).

Firstly, before calculating brightness temperature, Digital Number (DN) values were converted to radiance with the following formula (Harrisgeospatial.com, 2017):

$$L_\lambda = \textit{Gain} * \textit{Pixel value} + \textit{Offset}$$

L_λ = Radiance in units of W/(m2 * sr * μm)

All images were downloaded as GeoTIFF with Metadata format and gain and offset values were obtained from the image's metadata. Accordingly, the spectral radiance values were converted to top of atmosphere (TOA) brightness temperature (Landsat 8 users' book, 2019):

$$T_B = \frac{K_2}{ln(1+\frac{K_1}{L_\lambda})}$$

where T_B is top of atmosphere brightness temperature (K), L is TOA spectral radiance (Watts/(m2 * srad * µm)), K1 and K2 are band-specific thermal conversion constants. Table 2.2 shows the constants, which were used in this study for each different satellite. These values were obtained from the metadata.

Table 2.2. The list of K1 and K2 constant values

Units	Watts / (m² * srad * µm	Kelvin
Constant	K1	K2
Landsat 5	607.76	1260.56
Landsat 7	666.09	1282.71
Landsat 8* * Band 10	774.89	1321.02

Thirdly, the NDVI threshold method was implemented. The brightness temperature obtained in the previous stage is also called black body temperature. Given this name, the temperature represents an object which absorbs all of the radiation, thus correction of spectral emissivity based on real object properties is needed. With using NDVI threshold method, image emissivity can be calculated as 3 different class regarding their NDVI values: If NDVI value is above 0.5 it represents dense vegetation and emissivity value is 0.99, and lower than 0.2 NDVI value represents bare soil and emissivity value is 0,97 and if NDVI value is range between 0.2 and 0.5 it represents soil/vegetation mixed area and emissivity value is calculated by following formula (Giannini et al., 2015) :

$$\varepsilon = \varepsilon_s * (1 - PV) + \varepsilon_v * PV$$

Where ε_s = 0,97 and ε_v = 0,99 and:

$$PV = \left(\frac{NDVI - NDVI_{min}}{NDVI_{max} - NDVI_{min}}\right)^2$$

Where $NDVI_{min} = 0,2$, $NDVI_{max} = 0,5$)

Fourthly, emissivity correction formula was applied using the emissivity values from the previous step, NDVI threshold method, with the following formula (Zhang et al., 2013):

$$T_s = \frac{T_B}{1 + (\lambda x T_B / \alpha) ln\varepsilon}$$

where: Ts is surface radiant temperature in Kelvin (K), TB is black body temperature in Kelvin (K), λ is wavelength of emitted radiance, and α = h.c/ (1.438 × 10−2 mK) (where h is Planck's constant (6.626 × 10−34 J s−1), c is the Velocity of light (2.998 × 108 m s−1), k is Boltzmann's constant (1.38 × 10−23 J K−1), and ε = Surface emissivity).

Finally, the temperature values were converted to Celcius with the following formula:

$$LST_{°C} = LST_K - 273.15$$

After retrieval of LSTs were completed, to compare the temperature variations between the images, line graphs were created from the mean temperature of each image.

2.1.3 Analyzing spatiotemporal changes of LST

Firstly, all LSTs were normalized by using the min-max normalization method.

$$LSTN = (LSTi - LSTmin) / (LSTmax - LSTmin)$$

where LSTN is the normalized value of pixel i; LSTi is the LST of pixel i; LSTmax is the maximum LST and LSTmin is the minimum LST in the image. Normalized LSTs were multiplied by 100 to simplify interpretation.

Secondly, three consecutive images for each period were averaged and LST maps were created.

2.1.4 Analyzing spatiotemporal changes of SUHI and LC

In order to delineate UHI areas, various UHI indices have been used in literature. In this study, the following formula which is created based on the definition of UHI, temperature difference between urban areas and the surrounding rural areas in the city's administrative boundary (Feng, Zhao, Chen and Wu, 2014) divided by the standard deviation, was used :

$$SUHI = Urban - Non\text{-}urban\ /\ Standard\ deviation$$

where Urban is represented by urban fabric; industrial, commercial and transport units; mine, dump and construction site. Non-urban areas are represented by artificial, non-agricultural vegetation areas; agricultural areas, forest and semi natural areas.

The index was applied to all images (15 images of 28 years from 1990 to 2018) for several analyzes. Firstly, the SUHI values were used to analyze the correlation between urban fraction and UHI relationship. Secondly, the SUHI changes against two different land cover; urban and agriculture were analyzed for all periods.

Finally, in order to analyze spatial distribution of SUHI areas, accumulated land cover change fractions against distance from the urban center were compared.

2.1.5 Classification of SUHI

Although min-max normalisation was applied, due to differences in weather conditions among the selected images, absolute LST values are not directly comparable. In order to eliminate the temporal variability of weather, Jenks Natural Break classification have been used for SUHI studies to classify LST among different images (Lin, Jim, Deng and Wang, 2018: Peng, Xie, Liu and Ma, 2016: Weng, Liu, Liang and Dengsheng Lu, 2008). Thus, Jenks Natural Break classification was applied to each image. This classification sets class intervals with iterative processes, until goodness of variance fit is maximized, so that variation within classes are minimized and variation among classes are maximized (Jenks, 1967). Each image was classified in five temperature categories as hot, warm,

neutral, cool, cold which adapted from the seven-point scale (ISO 10551, 1995) temperature classes.

The classified three consecutive LST values were merged using cell statistics for each period. Overlay statistic was chosen as median, which assigns the median value for each pixel on a cell-by-cell basis ("How Cell Statistics works—Help | ArcGIS for Desktop", 2019). Thereby extreme values among the each period were refrained.

2.1.6 Relationship between SUHI and land cover changes

To better understand the relationship between SUHI and land cover, the CORINE Land Cover Change (CHA) so called change layer product was used. The reason for using CHA instead of change between CLC is that change layers were created for the comparison purpose and has a higher resolution (minimum mapping unit 5 ha, for CLC 25 ha) than CLC. The comparison was conducted between every two consecutive periods by using the CHA product. The UHI values for every two consecutive periods extracted by the corresponding CHA mask.

The comparison was conducted between every two consecutive periods by using the CHA product. The UHI values for every two consecutive periods extracted by the corresponding CHA mask.

Originally, 35 different land cover changes formed between the five periods. However, to make the analysis more effective, based on the classification created for this study (Table 1), the CHA maps were classified into 7 different classes: interchanged, urban to green urban, rural to green urban, urban to rural, unchanged, urbanized. Interchanged indicates changes within the artificial surfaces (11,12,13). Urban to green urban indicates changes from artificial surfaces (11, 12, 13) to green urban (14). Rural to green urban indicates changes from rural areas (20) to green urban (14). Urban to rural indicates changes from artificial surfaces (11, 12, 13) to rural areas (20) and forest and semi-natural areas (30). Unchanged indicates the changes between the level II categories.

Urbanized indicates changes from rural areas (20), green urban (14), forest and semi-natural areas (30) to artificial surfaces (11,12,13).

2.3 Results and Discussion

2.3.1 Spatiotemporal changes in land cover
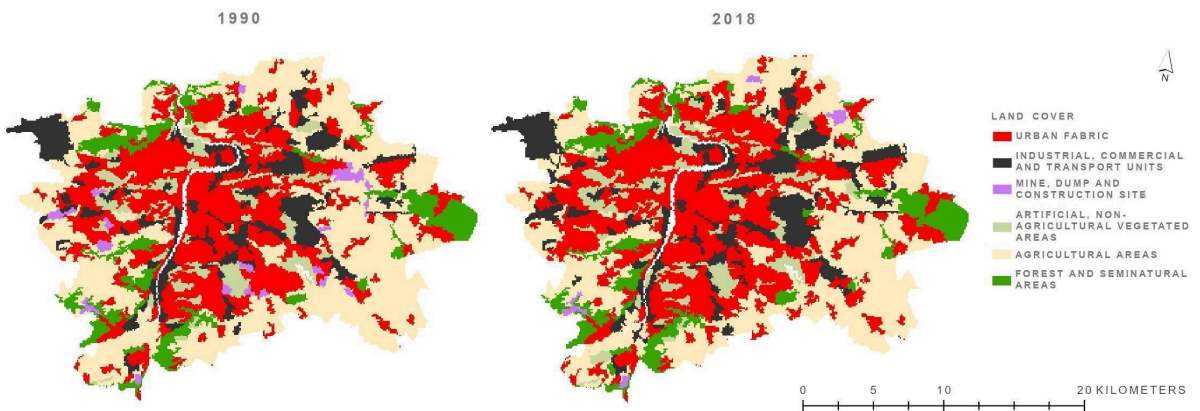
Figure 2.2. The spatial pattern of land cover maps for 1990 and 2018.

Figure 2.2 reveals that there have been no distinctive changes between 1990 to 2018. The most prominent change can be seen in mine, dump and construction sites which were replaced by urban fabric. Another prominent difference can be seen in the north-east part of the city, changes from arable land to industrial, commercial and transport units. Overall, with the consideration of the city's size, in terms of spatial pattern, the changes are not dramatic for a 28 year period.
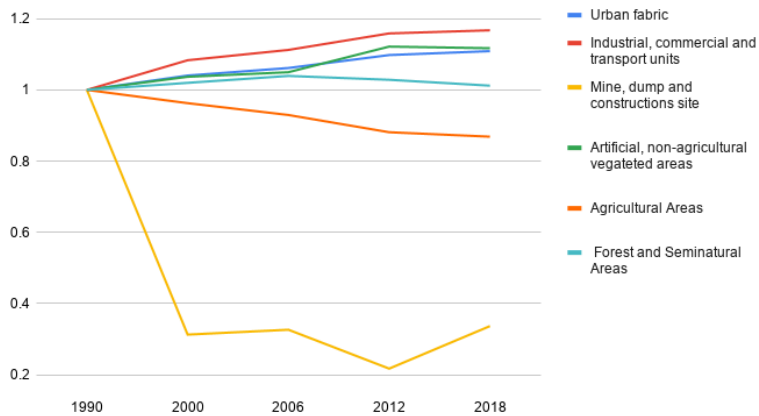
Figure 2.3. The ratio of relative land cover changes compared to 1990 (right).

Multitemporal analysis of the land cover changes of all periods relative to 1990, is displayed in multiple line graphs (Figure 2.3). Mine, dump and transport units decreased rapidly until 2000, fluctuating between 2006 and 2012, though there was an overall decrease of nearly 333%. The graph shows that there has been a gradual increase in urban fabric, industrial, commercial and transport units and for all periods. On the contrary, it is shown that agricultural areas decreased steadily, though the rate of decrease declined for the period 2012-2018. Forest and semi natural areas, increased slightly until 2006 and decreased for the rest of time span, so overall increase of 1%. Artificial non-agricultural vegetation areas increased, though there was a slight decrease between 2012-2018.

Overall, for the period 1990-2018; urban, industrial and artificial vegetated areas have been increased by replacing the agricultural areas and mine, dump and construction sites.

2.3.2 Spatiotemporal changes of LST

Figure 2.4 shows the LST patterns in 1990 and 2018. Although the spatial pattern of SUHI for these periods are similar, it can be seen that the highest LST areas were expanded between two periods. Especially the northeast and northwest part of the city, which is categorized as industrial, commercial and transport units (see Figure 2.3). Accordingly, it can be said that LST increases parallel to expansion of artificial

43

surfaces. However, LST patterns are not distinguishable from these maps and detailed interpretation is not possible. This limitation reveals the necessity of further classification.
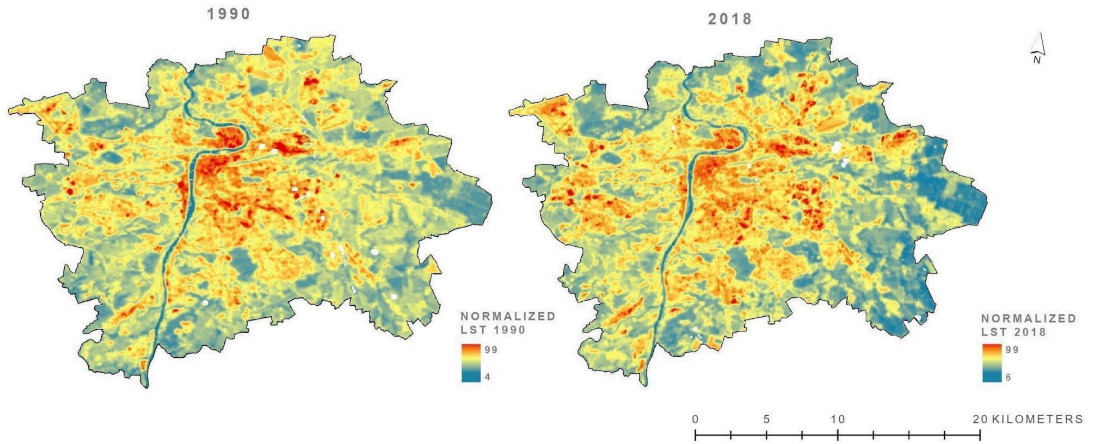
Figure 2.4. Spatial patterns of the LST for Prague for 1990 (left) and 2018 (right)
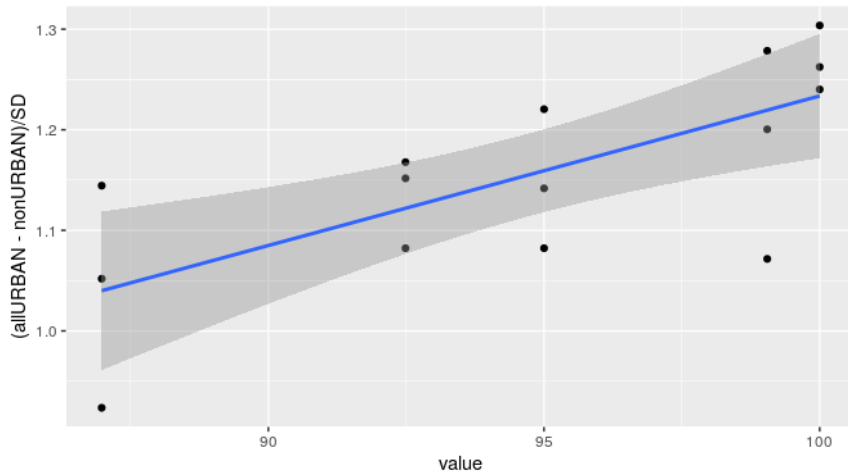
Figure 2.5. SUHI intensity and urban fraction relation, all images.

Correlation analysis between urban fraction and SUHI revealed a significant correlation (see Figure 2.5).
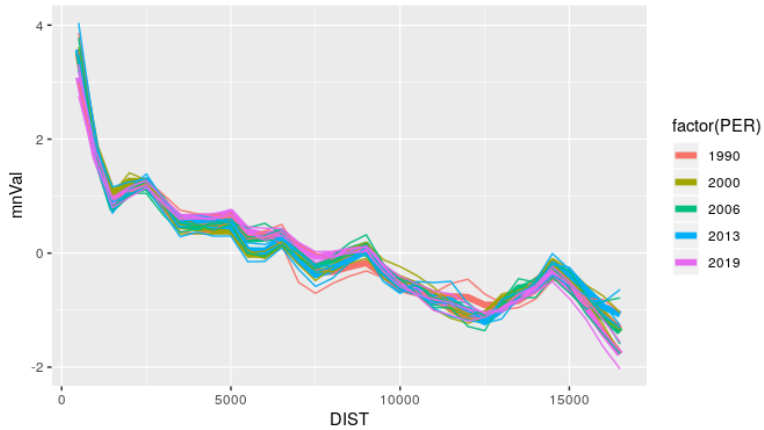
Figure 2.6. SUHI intensity changes against distance from the urban center, all images.

Figure 2.6 shows the SUHI intensity decreases with the distance from the urban center. In order to analyze the effect of land cover changes, SUHI intensity changes against land cover fractions were compared for all periods (see Figure 2.7). The results show that SUHI intensity and agriculture areas have a negative relationship. Conversely, SUHI intensity and urban fabric has a positive relationship.
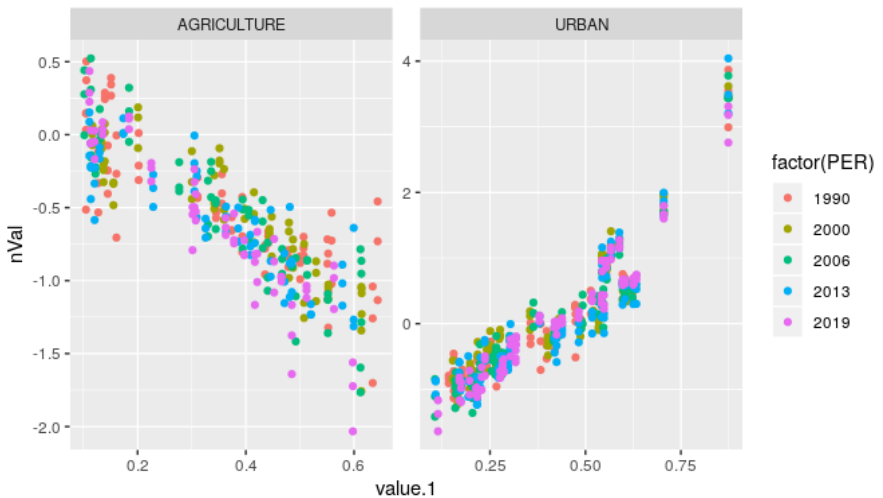
Figure 2.7. UHI intensity changes against land cover fractions, all periods.

2.3.3 Surface Urban Heat Island Intensity

The results of the classified SUHI intensity analysis for 1990 and 2018 are displayed in Figure 2.8. The SUHI spatial patterns show that hot regions are highly clustered in the urban center, along the river and radiated dispersedly around it. From 1990 to 2018 the hot regions are expanded and surrounded by warm regions extensively. Fig. 10 also demonstrates the extent of SUHI intensity classes and the graph shows that there has been a gradual increase in hot and warm regions contrary to cool and cold, between 2006 and 2018.
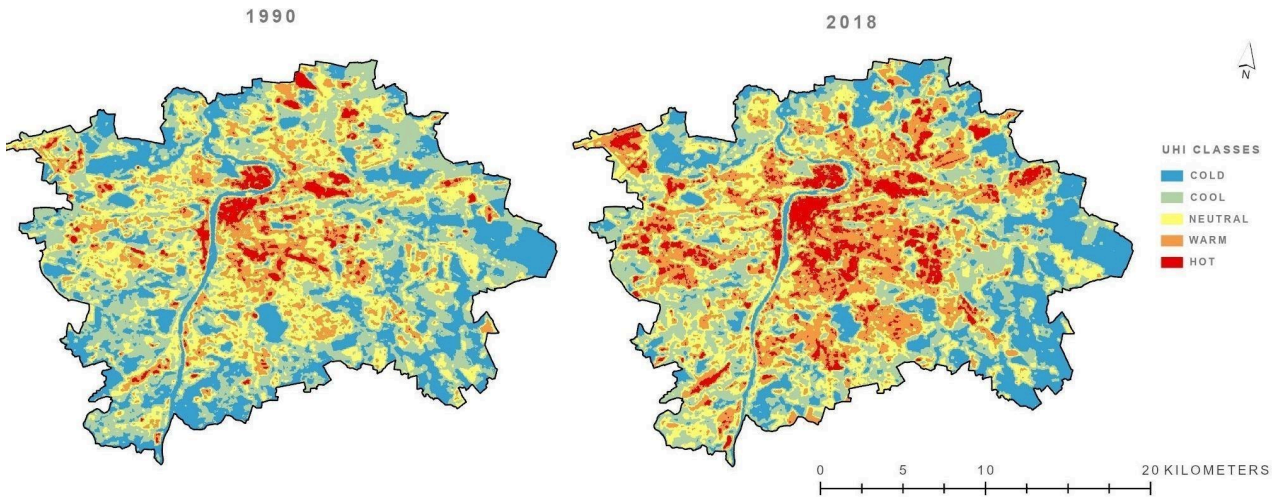
Figure 2.8. Spatial patterns of the SUHI intensities for Prague for 1990 (left) and 2018 (right).
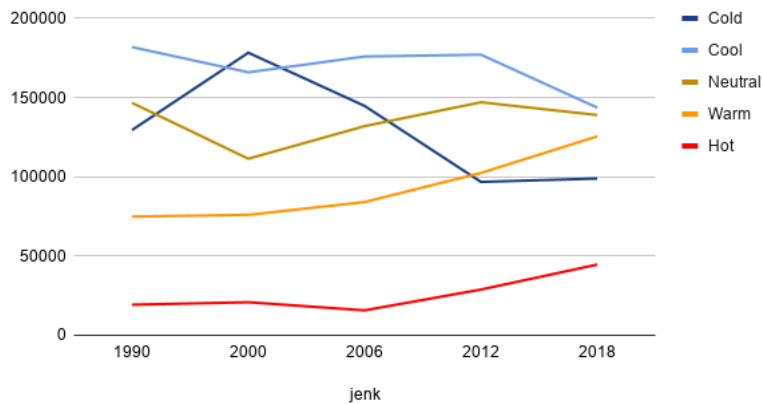
Figure 2.9. SUHI intensity changes.

Compared to the land cover maps, the similarity between land cover pattern and SUHI classes is evident. The method used in this study, to combine classified SUHI maps with using cell statistics median choice, can be used as a viable alternative for dealing with the issue of using several images to represent a period.

2.3.4 Surface Urban Heat Island Intensity
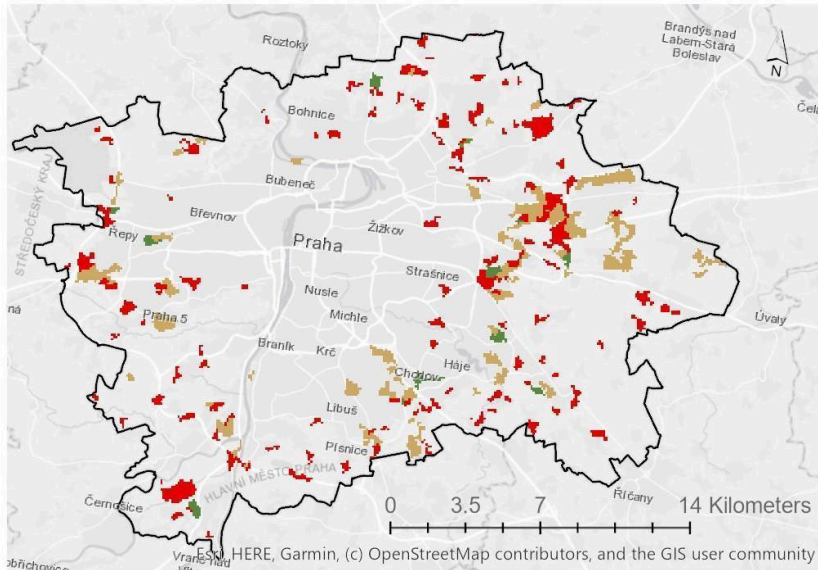
Figure 2.10. Changed areas between 1990 to 2018.

The results of the difference in land cover fractions against distance from the urban center analysis is displayed in Figure 2.11. The graph shows that a significant proportion of land cover changes were formed mainly on the outskirts of the city, between 9 km and 12 km distance from the center. However, fluctuations start at the 5 km distance and continue till the end of the city boundary. Similarly, the spatial distribution of the changes in the study area shows that the changes were formed far from the city center with various sizes and proximity to each other (see Figure 2.10). These results indicate the peri-urbanization that mostly increases the extent of the SUHI area.
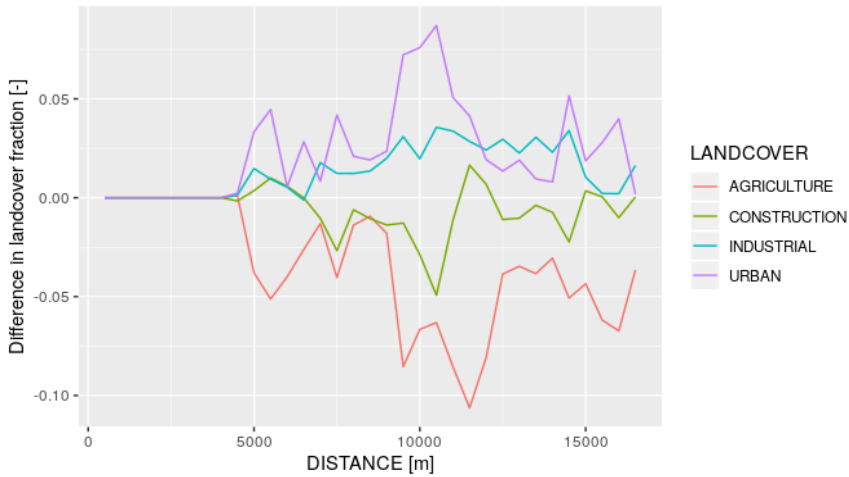
Figure 2.11. Land cover fractions against distance from the urban center, accumulation of all periods (left).

Table 3 summarizes UHI classes change by land cover change between the five periods. In most cases, interchanged areas didn't affect UHI level except changes to industrial, commercial and transport units which elevated UHI. Similarly, two thirds of urban to green urban changes didn't affect UHI while one third of lowered UHI. Likewise, changes from urban to rural areas lowered UHI. On the contrary, three fourths of urbanized areas elevated UHI up to two levels while one fourth didn't. On the other hand, unchanged areas didn't affect UHI.

Overall, the results of the changes from artificial surfaces to green urban and rural lowered UHI, conversely, changes from rural to artificial surfaces elevated to UHI.

Spatial distribution of these changes are shown in Fig.11, the location and size of land cover changes are varied. Interestingly, the results show that the same category of changes effect on UHI varies from no change to up to two level change. This can be explained by other factors which affect the formation and intensity of UHI such as surrounding areas, topography and sky view factor, weather conditions (wind direction and speed). In accordance with the present results, previous study (Wu, Zhang and Zang, 2019) have demonstrated that UHI depends not only on land cover but also elevation, population density of the location. However, the results of

this study do not explain the other factor which affects the UHI. Further research, which takes them into account, will need to be undertaken.

Table 2.3. Land cover changes (old and new land land cover) and corresponding SUHI classes.

	Change	Old CLC	New CLC	1990	2000	2000	2006	2006	2012	2012	2018
IC	Interchanged	11	12	4	5			4	4		
		11	13	2	2			3	3		
		13	11	4	4	3	3				
		13	12	3	4	4	3	2	4		
UG	Urban to green urban	11/12/13	14	4	4	3	3	4	3		
RG	Rural to green urban	20	14					3	3		
UR	Urban to rural	12	20			4	2				
		13	20	3	3	4	3	4	3		
		13	30			3	2	4	3		
UC	Unchanged	13	13					4	4		
		20	20	2	2	2	2	2	2		
		20	30			3	3				
		30	30	1	1					2	2
U	Urbanized	14	11	3	3	3	4				
		14	12	2	5	3	4			2	3
		14	13			4	4	2	3		
		20	11	2	3	2	3	2	3	3	4
		20	12	3	4	2	4	2	3	3	3
		20	13	3	3	2	3	3	3	4	4
		30	11					3	4	3	3
		30	12					3	4		

2.4 Conclusion

This paper has analyzed the effect of land cover changes on the Urban Heat Island (UHI) phenomenon in Prague. The analysis utilized CORINE land cover and Landsat images from the years 1990, 2000, 2006, 2012, and 2018. The results indicate that arable areas have been progressively replaced by urban fabric over the years, leading to an increase in the Surface Urban Heat Island (SUHI) level.

Interestingly, the majority of these land cover changes did not occur in the city center but rather at a distance of 9 km to 12 km from it. This peri-urbanization, or urbanization in the hinterland of the city, resulted in an expanded extent of the hot and warm SUHI classes. A comparison of land cover changes and SUHI classes revealed that the effect of the same land cover changes on SUHI varied across different locations.

In conclusion, both qualitative and quantitative analysis show that the extent of SUHI in Prague has increased as a result of peri-urbanization. It is recommended that urban planners and decision-makers consider the impact of land cover change, along with other factors affecting SUHI, in their planning and decision-making processes. Furthermore, the adoption of green infrastructure and sustainable urban planning strategies could potentially mitigate the effects of SUHI, enhancing the livability and resilience of urban areas in the face of climate change.

2.5 Appendix A

Table A.1. List of Landsat images and acquisition times.

Number	Date	GMT+2	GMT
1	19910706	11:20	09:20
2	19910807	11:20	09:20
3	19910816	11:14	09:14
4	19990705	11:28	09:28
5	20000605	11:27	09:27
6	20000620	11:48	09:48
7	20050603	11:38	09:38
8	20050728	11:45	09:45
9	20070625	11:44	09:44
10	20110604	11:40	09:40
11	20130727	11:52	09:52
12	20130803	11:59	09:59
13	20170611	11:56	09:56
14	20170620	11:50	09:50
15	20190626	11:50	09:50

Chapter III

Case Study II: Effect of COVID-19 Lockdown on Urban Heat Island Dynamics in Prague, Czechia

Tugba Dogan, Aleš Urban, Martin Hanel

Abstract

Urban heat island (UHI) is a well-known phenomenon adversely affecting human health and urban environments. The worldwide COVID-19 lockdown in 2020 provided a unique opportunity to investigate the effects of decreased emissions of air pollution and anthropogenic heat flux (AHF) on UHI. Although studies have suggested that reduced AHF during lockdown decreased atmospheric UHI (AUHI) and surface UHI (SUHI), these results contain inherent uncertainties due to unaccounted weather variability and urban-rural dynamics. Our study comprehensively analyzes the impact of the COVID-19 lockdown on AUHI and SUHI in Prague, Czechia. By selecting days with similar weather conditions, we examined changes in mean SUHI using MODIS satellite images and in AUHI based on air temperature from Prague weather stations for the Lockdown period during March–April 2020 versus a Reference period from March–April 2017–2019. Our results show that, in comparison to the Reference period, the Lockdown period was associated with a 15% (0.1 °C) reduction of SUHI in urbanized areas of Prague and a 0.7 °C decline in AUHI in the city center. Additionally, the observed decreases in satellite-based Aerosol Optical Depth and Nitrogen Dioxide by 12% and 29%, respectively, support our hypothesis that the weakened UHI effects were linked to reduction in anthropogenic activities during the lockdown. Revealing the largest decrease of mean SUHI magnitude in the periphery of Prague having predominantly rural land cover, our study emphasizes the need to consider the effects of urban-rural dynamics when attributing changes in SUHI to AHF. Our findings provide additional insights into the role of reduced anthropogenic activities in UHI dynamics during the COVID-19 lockdown and offer policymakers a comprehensive understanding of how the complex interaction between urban and rural microclimate dynamics influences the SUHI phenomenon.

Keywords: urban heat island; surface urban heat island; anthropogenic heat flux; land surface temperature; COVID-19 lockdown

3.1 Introduction

Coronavirus disease (COVID-19) caused by the severe acute respiratory syndrome coronavirus 2 (SARS-CoV-2) emerged in Wuhan, the capital of Hubei Province, China, early in December 2019, then spread globally within several months. The World Health Organization declared the COVID-19 outbreak a pandemic on 11 March 2020. Extraordinary measures were implemented around the world to slow the spread of the virus, ranging from closures of services, schools, and universities to national curfews.

The implementation of COVID-19 lockdown measures led to a significant reduction in human activities and mobility. This, in turn, caused a decrease in anthropogenic emissions, which subsequently led to a rapid improvement in air quality in locations across the globe (Muhammad et al., 2020; Kumari and Toshniwal, 2020; Liu et al., 2021; Venter et al., 2020). For example, based on the Google mobility index and satellite data (Sentinel-5P), 90% reduction in mobility and 30% decline in NO_2 emissions were observed in six countries across the northern hemisphere due to lockdowns in March 2020 (compared to March 2019) (Muhammad et al., 2020).

Similarly, studies using ground observations reported as much as 34%, 47%, and 64% reductions in $PM_{2.5}$, PM_{10}, and NO_2 concentrations, respectively, in cities across the globe due to restrictions on anthropogenic emission sources during the lockdown (Muhammad et al., 2020; Kumari and Toshniwal, 2020; Liu et al., 2021; Venter et al., 2020). Furthermore, reduction in CO_2 emissions during the lockdown during March–April 2020 has been documented on global (8.8%, (Liu et al., 2021)) as well as local scales (e.g., a drop by 30% in the San Francisco Bay Area (Potter and Alexander, 2021)). The drop in CO_2 was attributable primarily to changes in traffic (Liu et al., 2021; Potter and Alexander, 2021).

Similar to the changes in air pollution, anthropogenic heat emissions likely decreased during the lockdown, as they are closely associated with the same human activities that release air pollutants. Anthropogenic heat flux (AHF) is one of the well-known causes of the urban heat island (UHI) effect (Fan and Sailor, 2005) and an important input parameter of the surface energy budget in urban areas (Oke et al., 2017). Unlike air pollution emissions and concentrations, however, AHF is challenging to measure; it needs to be estimated from such other proxy variables as air pollution (Lee et al., 2014), energy consumption data (Chen and Hu, 2017), or land surface temperature (LST) (Firozjaei et al., 2020). The near-surface thermal microclimate of a given site is defined by the surface energy balance equation with the following equation:

$$Q^* + QF = QH + QE + \Delta QS + \Delta QA \qquad (1)$$

where Q^* is net all-wave radiation, QF is AHF density, ΔQS is net heat storage, ΔQA is net advective heat flux, QH is sensible and QE is latent heat flux density (Oke, 1987; Oke et al., 2017). The two turbulent heat flux densities, sensible and latent heat flux, facilitate the energy transfer between the surface and the atmosphere (Lee, 2017; Oke et al., 2017). AHF is an added energy input to the energy balance that impacts primarily thermal characteristics of the urban canopy layer. However, authors agree that AHF is also an important driver of LST due to enhanced heat exchange between the atmosphere and urban land surfaces (Feng et al., 2023; Hamilton et al., 2009; Lee, 2017; Liu et al., 2022; Oke et al., 2017; Firozjaei et al., 2020). Hence, it is hypothesized that the reduction in AHF during the COVID-19 lockdown led to a weaker UHI effect and a decreased magnitude of the surface UHI (SUHI) (Feng et al., 2023; Meng et al., 2023; Mijani et al., 2023; Pal et al., 2021).

Since the outbreak of the COVID-19 pandemic, there has been a growing body of literature on the effects of lockdowns on UHIs (Chakraborty et al., 2021; Liu et al., 2022; Parida et al., 2021). A recent review of 29 studies on urban temperature anomalies during the COVID-19 lockdown revealed a decrease in UHI, LST, or SUHI, respectively, in the majority of 46 cities across various regions and climate zones (Wang and He, 2023). The average LST decrease in developed (i.e. mid- and high-latitude) countries

was smaller than that in developing countries, which is in line with findings from China (Liu et al., 2022) where the UHI-decline effect related to the lockdown weakened with increasing latitude.

Another global study suggests that while there was a substantial decrease in the SUHI magnitude of Chinese cities, the results from Europe and USA were less significant (Sismanidis et al., 2023). Similar patterns were observed in a study comparing LST in Europe and North America during March–May 2020 to the same period in 2015–2019 (Parida et al., 2021). The decrease in LST was generally larger in urban areas compared to rural landscapes, suggesting weakening SUHI effects, especially during nighttime. On the contrary, daytime LST increased over large parts of Europe due to less attenuation of solar radiation by atmospheric aerosols and anticyclonic synoptic conditions over Europe during the lockdown period (Parida et al., 2021; Glocke et al., 2023). These findings highlight the importance of taking into account the spatial and temporal variability in synoptic conditions when analyzing and comparing temporal changes in SUHI.

Indeed, while the aforementioned studies offer important insight into large-scale effects of the COVID-19 lockdown on LST and SUHIs, they mostly neglect within-city differences between urban and rural land cover types and the way they are affected by day-to-day weather variability (Parida et al., 2021; Glocke et al., 2023). Distinguishing between urban and rural microclimate dynamics and controlling for the effect of natural weather variability are, however, crucial steps in identifying changes in SUHI attributable to variations in AHF (Chakraborty et al., 2021). While urbanized areas are largely affected by anthropogenic heat, rural areas are more susceptible to changes in weather conditions. Nevertheless, most studies do not take into account this effect when assessing impacts of COVID-19 lockdowns on SUHIs and attribute all changes in cities to anthropogenic heat. In order to attribute the changes in SUHI more precisely to AHF variability, it is necessary to control for the effects of synoptic conditions. This can be achieved via a rigorous process for selecting study period based on synoptic conditions and evaluating the results by taking into account the local dynamics as well.

In this study, we aim to assess the effect of the COVID-19 lockdown during March 2020 on UHI dynamics in Prague, Czechia. In order to determine the changes in SUHI magnitude, we used MODIS satellite images for 8 selected days within the main lockdown period during March–April 2020 and 10 selected days during March–April 2017–2019. To ensure consistent synoptic conditions, only days with similar weather parameters were selected. SUHI magnitude was defined as the difference between urbanized areas (i.e., areas within the city having artificial land covers) and selected rural areas (i.e., areas within the city having typically rural land covers). Furthermore, to provide a more comprehensive picture of UHI patterns during the lockdown period, we cross-validated the change in SUHI magnitude during the lockdown period with i) atmospheric UHI (AUHI) changes calculated from selected Prague weather stations, and ii) changes in air pollution concentrations obtained from Sentinel-5's TROPOMI and MODIS's Aerosol Optical Depth products.

Our study presents a novel approach to decouple confounding factors from the potential impact of AHF variations on UHI dynamics. First, we introduced robust image selection criteria to minimize the effect of synoptic variability and changes in global radiation during the lockdown period. Furthermore, by distinguishing urbanized and rural areas within the city boundaries, we were able to control for the confounding effects of contrasts and interactions between urban and rural microclimates (referred to as urban-rural dynamics) on the changes in SUHI magnitude. Finally, by investigating the effect in zones of Prague, we were able to explain the association between the level of urbanization and other factors influencing UHI. Employing this approach, our study provides new insight into attributing UHI dynamics during the COVID-19 lockdown to the role of AHF while considering intra-urban microclimate variations between urban and rural areas.

3.2 Materials and Methods

3.2.1 Study Area

Prague is the capital city of Czechia. It is located at approximately 50° 4' north latitude and 14° 25' east longitude. The city covers an area of 496.2 km². According to the Köppen classification, Prague experiences a temperate oceanic climate (Cfb) that is characterized by distinct seasons with relatively mild temperatures and moderate rainfall throughout the year (Kottek et al., 2006). The population of Prague reached 1.33 million in 2020, and this has not changed substantially in recent years (Czech Statistical Office, 2023).

3.2.2 Data

Table 1 presents all datasets used in the analysis. For the assessment of SUHI dynamics, we used daily LST variables obtained from NASA's Moderate Resolution Imaging Spectroradiometer (MODIS) program. The CORINE Land Cover 2018 product was used to identify urban and rural land cover categories within the city of Prague. Additionally, we employed MODIS's Aerosol Optical Depth (AOD) dataset and the Offline Nitrogen Dioxide (OFFL NO2) product of Sentinel 5 Precursor to analyze changes in air pollution concentrations. All remote sensing data were downloaded and processed via the Google Earth Engine catalog.

Table 3.1. Datasets used in this study.

Category	Variables	Temporal and Spatial Resolution	Data Source
LST – MODIS day	LST_Day_1km	daily, 1 km	National Aeronautics and Space Administration
AOD – MODIS	Optical_Depth_055	daily, 1 km	National Aeronautics and Space Administration
NO_2 – Sentinel 5	tropospheric_NO2_column _number_density	daily, 1 km	European Space Agency
Land cover – CORINE	CLC2018	minimum mapped unit of 25 ha	European Space Agency
Weather station	air temperature global radiation	hourly daily	Czech Hydrometeorological Institute

The final analysis of LST and SUHI spatial dynamics was conducted in the ArcGIS 11 software. Records of hourly temperature, cloud cover, precipitation, and daily mean global radiation from four professional weather stations in Prague (Praha-Karlov, Praha-Kbely, Praha-Libus, and Praha-Ruzyne; Figure 1), managed by the Czech Hydrometeorological Institute, were used to control for synoptic conditions and changes in AUHI. Three concentric zones of Prague (Inner City, Outer City, Periphery), based on urbanization level and demographic spatial patterns (Ouředníček, 2022), were used to relate the changes in SUHI to anthropogenic activities (Figure 3.1, Table 3.2).
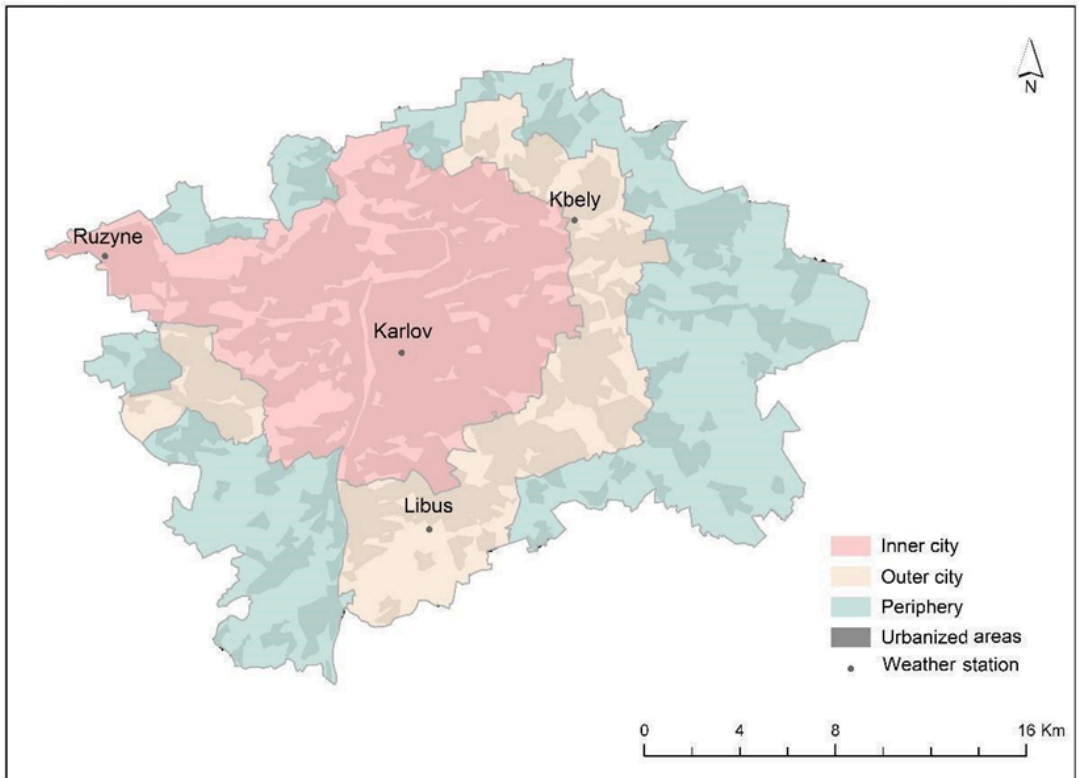
Figure 3.1. Three concentric zones of Prague (Ouředníček, 2022) and locations of weather stations used in this study.

Table 3.2. Characteristics of the three concentric zones of Prague as defined in Figure 1 (Ouředníček, 2022).

Zone	Area (km²)		Population count		Population density (inhab/km²)
Inner City	173.6	35.0%	727 589	60.9%	4 651
Outer City	115.1	23.2%	370 106	27.9%	3 216
Periphery	207.5	41.8%	146 656	11.1%	707
Prague (total)	496.2	100.0%	1 324 277	100.0%	2 669

3.3. Methods

In order to assess effects of the COVID-19 lockdown on Prague's UHI, we compared temperature and air quality conditions during the lockdown period with a selected reference period following the workflow in Figure 2. This workflow was implemented for the lockdown and reference periods separately. The results were then compared. Lockdown-related changes in SUHI were compared in the three concentric zones of Prague as described in Table 3.2. As the highest population density is in Inner City and the lowest is in Periphery, the largest decrease in SUHI can be expected in Inner City followed by Outer City and the smallest in Periphery. Details of the individual steps are explained below.
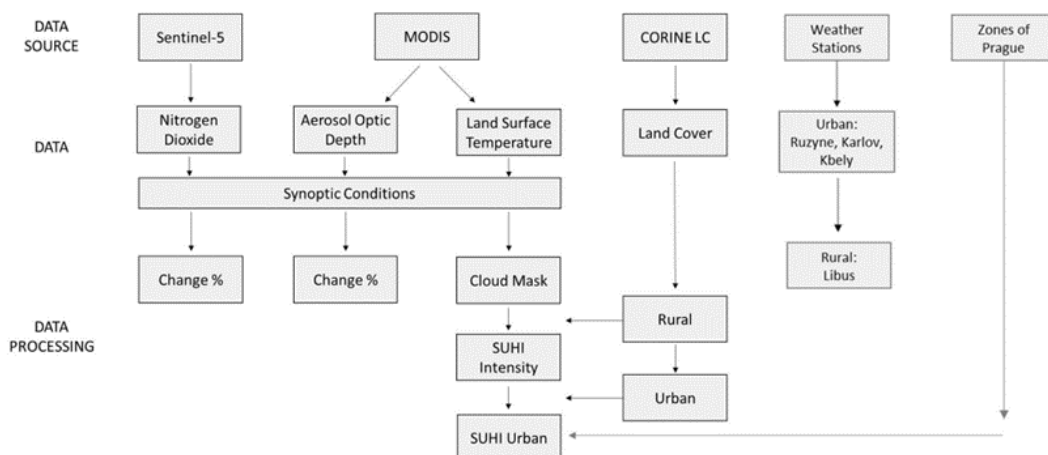
Figure 3.2. Workflow of the study.

3.3.1. Determination of the Study Period and Satellite Image Selection

Consistent with other countries' prevention strategies, declaration of a lockdown was necessary to limit the spread of COVID-19 after its outbreak in Czechia. A state of emergency was declared on 14 March 2020. A countrywide lockdown with the most stringent measures began 2 days later and lasted until the end of April (Our World in Data, 2023).

Lockdown measures (including closure of services, schools, places of employment, and retail sales; restrictions upon mobility between regions and public gatherings; etc.) dramatically affected human lifestyles, especially in urban areas. For example, data from Václav Havel Airport in Prague report an almost 80% decrease in the number of checked-in passengers in 2020 compared to 2019 (and the same decrease in the number of flights). This not only affected traffic at the airport per se but also influenced general tourism-related mobility in the city (Letiště Praha, 2023). Accordingly, overall traffic intensity in Prague dropped by more than 30% during the spring of 2020 compared to usual rates in 2019 before returning to nearly usual levels in the summer (Ročenka dopravy Praha 2020, 2023).

To identify changes in SUHI magnitude due to the lockdown, we selected MODIS Aqua satellite images acquired during the effective lockdown period defined from the start of the most stringent measures (16 March) to the 3rd wave of the loosening of measures (27 April), after which the relaxation plan accelerated (Our World in Data, 2023). To ensure that the comparison of lockdown versus reference periods was minimally affected by weather variability, we selected satellite images reflecting weather characteristics as similar as possible. In the first step, we filtered satellite images with total cloud cover over the Prague area with less than 45% coverage and used their temperature range (as defined by daily temperature data from Prague weather stations) as a benchmark to filter images in the reference period. In addition, conditions antecedent to image acquisition were also considered. Therefore, images with high cloud cover before acquisition and/or precipitation recorded a day before acquisition were excluded from the analysis. Additionally, we used daily global radiation records as a proxy for solar radiation to control for changes in radiative fluxes due to natural covariation of weather patterns and atmospheric composition during the lockdown (Parida et al., 2021; Liu et al., 2022). Due to the limited number of available images and a lack of established thresholds in the literature for similar studies, we listed relevant variables for the available images and excluded outliers. This way, we ensured that background conditions in the two periods were comparable and the observed changes in LST were attributable to changes in human activities and AHF.

As a result, 8 satellite images from the period 14 March–27 April were selected and defined as Lockdown. The dates of selected satellite images and their temperature and global radiation values are listed in Table A1. To avoid significant changes in land cover, we only chose days from the previous 3 years, 2017, 2018, and 2019, as the reference period. Using the same criteria as for Lockdown, 10 images from the previous three spring seasons (March–April 2017–2019) were selected and defined as Reference (Table B1). The same days were selected for the comparison of air temperature data (Section 3.4).

3.3.2. Land Surface Temperature Estimation

Land surface temperatures were derived from the Aqua satellite's Moderate Resolution Imaging Spectroradiometer (MODIS) sensor (MYD11A1, version 6.1) with 1 km resolution over Prague. Aqua satellite images were acquired at ~13:30 local solar time. For LST, the "LST_Day_1km" dataset and for quality assessment, the "QC_Day" layer were used. Nighttime LST data was not used due to high cloud percentages. Detailed methods for the LST algorithm and layers used are described in the MODIS documentation (Wan, n.d.).

3.3.3. Surface Urban Heat Island Magnitude Calculation

To quantify the dynamics of SUHI within a city, selection of the reference rural land cover area requires careful consideration. In this study, we used Pastures (class 231) and Transitional woodland-shrub (class 324) land cover types from the CORINE land cover data (CORINE Land Cover, 2023) as reference LST_{rural} (Oke, 1987). Thus, day-to-day weather variability was captured and the thermal characteristics of individual images were more comparable.

The SUHI magnitude of each MODIS image was calculated according to the following formula:

$$\text{SUHI magnitude} = LST_{image} - LST_{rural}, \qquad (1)$$

in which LST_{image} represents the LST in each pixel of the selected image and LST_{rural} is the mean value of the rural reference of the corresponding image.

Median SUHI magnitude values were computed for all images from the Lockdown period ($SUHI_{lockdown}$) and the Reference period ($SUHI_{reference}$). Consequently, $SUHI_{lockdown}$ and $SUHI_{reference}$ values were extracted separately for "urbanized areas" (defined as CORINE land cover classes continuous and discontinuous urban fabric, industrial or commercial units, road and rail networks and associated land, port areas, and airports) and changes in SUHI magnitude between Lockdown and Reference periods related to urbanized areas in the three concentric zones

of Prague (see Figure 1) were compared. In this way, changes in SUHI were quantified while controlling urban-rural dynamics and the level of human activities.

3.3.4. Analyzing Atmospheric Urban Heat Island

We used the mean hourly temperature records at 13:00 and 14:00 CET (T14) from the four Prague weather stations (Figure 1) to analyze the changes in daytime AUHI during Lockdown. Records at 13:00 and 14:00 CET were used, as these are most consistent with the time of MODIS image acquisition. Because Ruzyne and Kbely are stations situated at two Prague airports (i.e., their records might have been affected by changes in their traffic load during the lockdown) and Karlov is located in Prague's city center near the main traffic artery called "Severojižní magistrála", we considered Libus a "rural" reference station least affected by anthropogenic influences. Consequently, we quantified the potential effect of Lockdown on temperatures in Karlov, Kbely, and Ruzyne, as their average T14 anomalies (AUHI magnitudes) vis-à-vis Libus on days included in the Lockdown and Reference periods (Table A1), respectively.

3.3.5. Analyzing Air Pollution

In addition to air temperature and LST, we analyzed two indicators of air quality based on satellite data to verify the changes in anthropogenic activities. We used the Copernicus Sentinel-5P TROPOspheric Monitoring Instrument (TROPOMI) sensor to estimate the changes in NO_2, and daily MODIS Aerosol Optical Depth (AOD) to estimate changes in particulate matter concentrations (LP DAAC - MCD19A2, 2023; Sentinel-5P OFFL NO_2, 2023).

For this purpose, we acquired images for the whole effective Lockdown period (16 March–27 April). Likewise, for the Reference period, we used the mean for the same period in 2017, 2018, and 2019 for MODIS AOD but 2019 for TROPOMI NO_2, as the latter product is not available from previous years.

3.4 Results

3.4.1 Atmospheric Urban Heat Island Analysis

Figure 3a shows the distribution of afternoon temperature (T14) observed at Prague weather stations during the Lockdown and Reference periods. On average, we observed lower temperatures for Lockdown than Reference at all stations, except for Libus. Only the suburban station in Libus was slightly colder during Reference, but the difference was insignificant (less than 0.1 °C). This finding suggests that this station was least affected by anthropogenic changes and can be used as a reference station for the AUHI analysis.
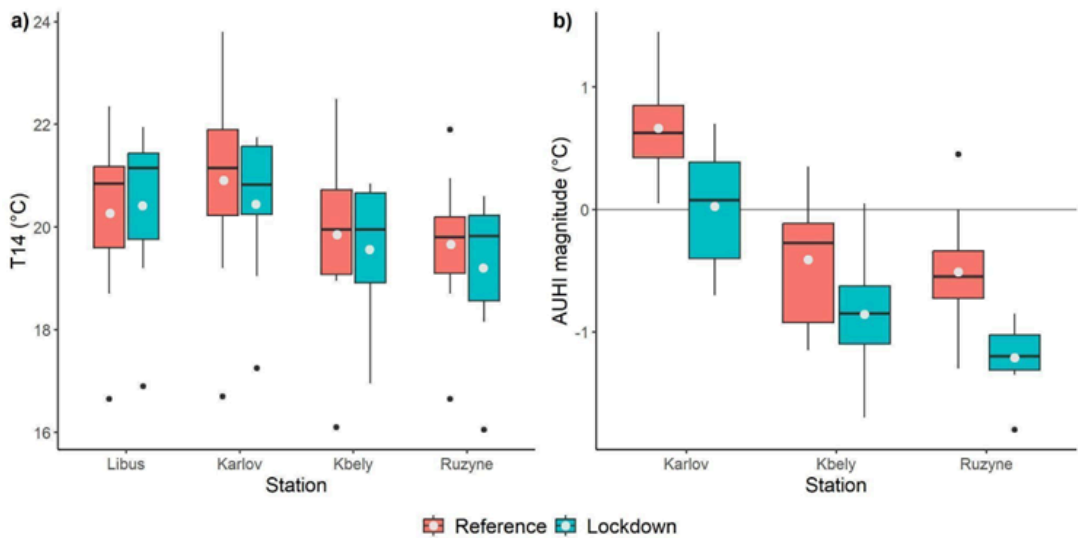
Figure 3.3. a) Afternoon air temperatures (T14) at four Prague weather stations during the Reference and Lockdown periods. b) Atmospheric urban heat island (AUHI) magnitudes calculated as T14 difference between a given weather station and the reference station in Libus. Box plots indicate medians and interquartile ranges of the values. Gray points denote mean values across all days in a given period at each station.

The results suggest that the AUHI magnitude decreased during Lockdown by mean 0.5 °C. The most important change observed in Karlov suggests a marginal (less than 0.1 °C) difference between the city center (Karlov) and its outskirts (Libus) during Lockdown, compared to 0.7 °C in the

Reference period (the change in AUHI magnitude was statistically significant according to the two sample t-test with p-value < 0.05). Although colder than Libus, the decrease in AUHI between Reference and Lockdown was comparable (0.7 °C, p < 0.01) at Ruzyne, while at Kbely it was only 0.4 °C (p = 0.1) colder.

3.4.2 Surface Urban Heat Island Analysis

While the results for AUHI suggested a significant decrease in UHI magnitude during Lockdown in Prague, we observed smaller changes in SUHI. Figure 3.4 shows the spatial distribution of SUHI magnitude in the whole domain city of Prague during the Reference and Lockdown periods. Both images indicated clear spatial clustering of areas with the largest SUHI magnitude (up to 3.5 °C) in predominantly urbanized areas (i.e., near the city center and important transport corridors) while periphery areas showed predominantly negative SUHI anomalies (by as much as −4.0 °C).
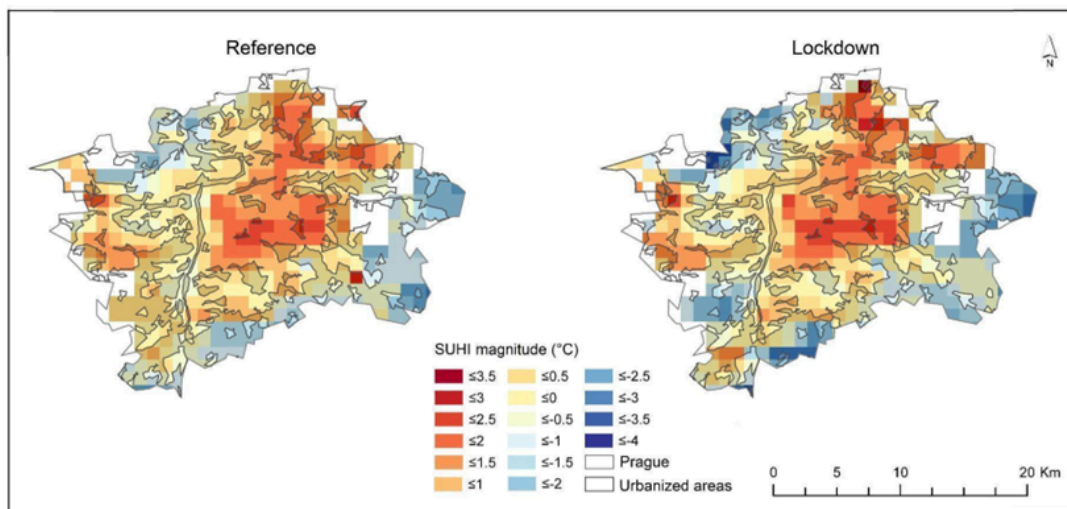
Figure 3.4. Spatial distribution of surface urban heat island (SUHI) magnitude during Reference (left) and Lockdown (right) periods in Prague based on Aqua satellite's Moderate Resolution Imaging Spectroradiometer (MODIS) sensor.

Figure 3.5 illustrates the spatial distribution of differences in SUHI magnitude between Lockdown and Reference. While the result indicates that some areas had stronger SUHI during Lockdown, mean SUHI

magnitude in Prague was 0.2 °C lower during Lockdown (Figure A1a). To investigate the potential effect of AHF, we analyzed the changes of SUHI in urbanized areas only (Figure A1b, Figure 5). The mean difference in SUHI magnitude between Reference and Lockdown in urbanized areas was 0.1 °C (i.e., 15% decrease). Contrary to AUHI magnitudes, the changes in SUHI magnitude were relatively small. However, histograms in Figure A1 suggest a generally lower frequency of pixels with positive SUHI magnitude during Lockdown. This suggests overall weakening of spatial SUHI magnitude in Prague during Lockdown.
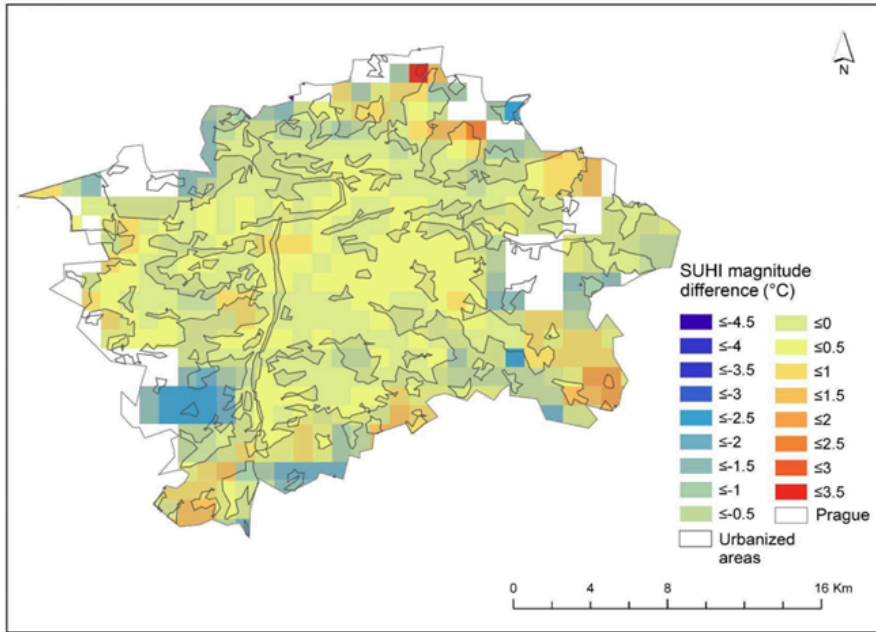
Figure 3.5. Spatial distribution of SUHI magnitude difference in Prague (Lockdown vs. Reference). Urbanized areas are brightened while rural areas are shaded.
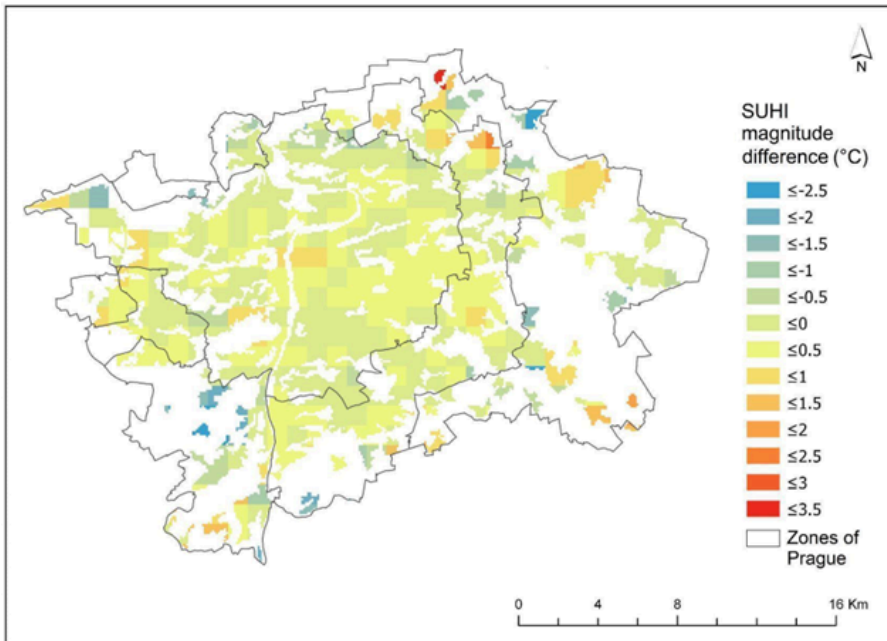
Figure 3.6. Spatial distribution of SUHI magnitude difference (Lockdown vs. Reference) in urbanized areas of the three concentric zones of Prague (Figure 3.1).

Table 3.3. SUHI magnitude changes in the three concentric zones of Prague during Lockdown.

Zone	Reference	Lockdown	Change (°C)	Change (%)	Change (%) / Population density (%)
Inner City	0.6	0.5	0.1	−17%	−31
Outer City	0.6	0.6	0	0	0
Periphery	−0.2	-0.4	−0.2	−100%	−1213

To analyze SUHI magnitude changes in the context of urbanization level and population density, a comparison was also made between the three concentric zones of Prague. Figure 3.6 shows the spatial distribution of SUHI magnitude differences in urbanized areas only. The SUHI magnitude difference for the three zones is presented in Table 3.3.

The largest decrease in SUHI magnitude was observed in Periphery. As this zone is characterized by the lowest population density and prevalence of agricultural land cover and forests (according to CORINE land cover classification: Figure A2), the SUHI magnitude was generally negative. The largest SUHI magnitude differences in this zone are related to the largest changes in the rural land cover types, especially in arable land and forests (Figure A3). As rural areas are generally more susceptible to both short-term (e.g., occurrence of rainy days before the image acquisition) and seasonal weather variability (e.g., beginning of the growing/seeding/harvesting season), we could observe the largest variance in SUHI magnitude in these classes (Figure A3).

On the other hand, Periphery is greatly affected by the daily commute from Prague suburbs to the city and intense flow of both national and international traffic on the highway circuit around the city. Furthermore, several industrial zones, such as a cement manufacturing plant in Radotín (the cool spot in the southwestern part of Prague in Figures 3.5 and 3.6), are located in Periphery. Thus, the changes in SUHI in this zone might

have been partly related to the significant drop in traffic intensity and AHF in these areas during Lockdown. However, given the 1 km resolution of MODIS images and linear character of the traffic-related activities, we were not able to get more precise information and we assume that most of the changes were related to the dynamics in rural areas within the city boundaries.

A 17% decrease in SUHI magnitude was observed in Inner City. This change was substantially smaller than that for Periphery. Inasmuch as industrial and urban fabric (Figure A2) cover more than 70% of the total area, however, and population density is highest in Inner City, we may assume that the reduction in SUHI magnitude in this zone was driven primarily by changes in human activities.

No significant change in SUHI was observed in Outer City, which can be characterized as a transition zone between Periphery and Inner City. Having a similar amount of industrial and urban fabric but higher population density (4.5 times as great) compared to Periphery, Outer City's negligible change in SUHI magnitude suggests that the decrease observed in Periphery was related rather to changes in the rural areas' dynamics than to AHF.

3.4.3 Air Pollution Analysis

In accordance with the AUHI analysis, a significant decrease in air pollution concentration was observed during Lockdown. Figure 3.7 shows differences in AOD and NO_2 concentrations between the Lockdown and Reference based on satellite data. Quantification of the changes in the three concentric zones of Prague is presented in Table 3.4.
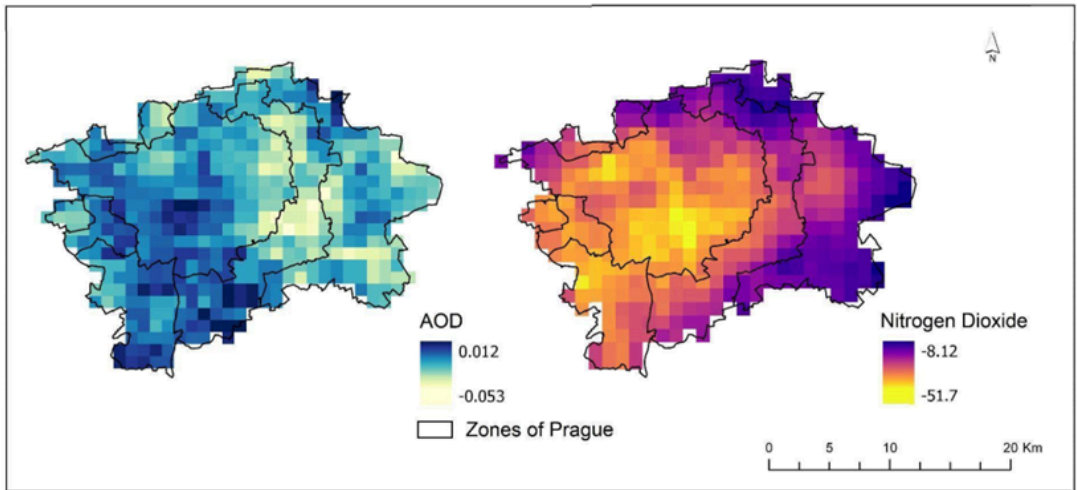
Figure 3.7. Difference in NO2 (left) and Aerosol Optical Depth (AOD) (right) concentrations (Lockdown vs. Reference).

Regarding NO2 concentrations, we observed an average decrease by 29% during Lockdown in 2020 compared to the same period in 2019. The decrease was largest in Inner City (3%), followed by Outer City (27%) and Periphery (25%). As NO2 concentrations are strongly related to traffic, these results support the hypothesis that SUHI magnitude changes in Inner City were more related to AHF variability, while changes in Periphery were driven by the rural dynamics.

Table 3.4. Difference in NO2 and Aerosol Optical Depth (AOD) concentrations in the three concentric zones of Prague.

Zone	NO$_2$ ($\mu mol/m^2$)				AOD			
	Reference	Lockdown	change	change (%)	Reference	Lockdown	change	change (%)
Inner City	147.7	111.1	−36.6	−32.9	0.103	0.092	−0.011	−10.8
Outer City	132.4	103.9	−28.4	−27.3	0.106	0.093	−0.012	−11.8
Periphery	124.2	99.1	−25.2	−25.4	0.105	0.091	−0.014	−13.3

Similarly, our analysis revealed a mean 12% decrease in AOD during Lockdown compared to the same period of 2017–2019. In contrast to NO2, the largest decrease was observed in Periphery (13%), followed by Outer City and Inner City (−12% and −11%), respectively. The generally

smaller percentage decrease in AOD compared to NO2 may be attributed to the longer reference period. Moreover, AOD is not a direct measure of a pollutant; instead, it represents the optical thickness of aerosols along a column of the atmosphere. Therefore, compared to the short-lived NO2, AOD is more influenced by long-range transport and the prevailing westerly winds in Prague that carry pollutants from the city center to the east (Patino and Duong, 2021; Simulated historical climate and weather data for Prague, 2023).

3.5 Discussion

In this study, we employed a comprehensive analytical approach to assess the effect of the COVID-19 lockdown on UHI dynamics in Prague, Czechia. We analyzed ground and satellite observations from the March-April 2020 Lockdown period and the March-April 2017-2019 Reference period. This analysis quantified changes in mean AUHI and SUHI magnitudes, as well as in air quality distribution, between the two periods. Our findings show that the COVID-19 lockdown in Prague was associated with: i) a 0.1 °C (15%) decrease in mean daytime SUHI magnitude over urbanized areas, ii) a 0.7 °C decrease in mean afternoon (13:00–14:00 CET) AUHI magnitude in the city center (Praha-Karlov weather station vs. the reference station in Praha-Libus), and iii) a 29% and 12% drop in mean NO2 and AOD concentrations, respectively, over the city.

Regarding changes in air temperature, our findings are in line with prior studies that observed weakened AUHI effects due to the COVID-19 lockdown. Similar to the results of our ground observations, an analysis performed with a high-accuracy observational network in Ghent, Belgium, revealed lower afternoon UHI magnitude (by as much as 0.4 °C/h) in the dense urban site during lockdown in 2020 as compared to the reference years (Hamdi et al., 2022). Likewise, a study across 300 cities in China observed a mean 0.42 K decrease in daytime AUHI magnitude due to lockdown (Liu et al., 2022).

Regarding SUHI changes, while some studies show a decrease similar to

our findings (Chakraborty et al., 2021; Liu et al., 2022; Roshan et al., 2021), others report an increase in SUHI effect during the lockdown (Feng et al., 2023; Parida et al., 2021). This discrepancy results from the large thermal variation for land surfaces, which depends largely on local synoptic conditions and spatial distribution of land cover types (Glocke et al., 2023). To better understand the underlying reasons for variations among results in previous studies and to comprehend the impacts of lockdown on SUHI and UHI better, the roles of anthropogenic heat and rural dynamics need to be elaborated.

3.5.1 Role of Anthropogenic Heat

Despite the solid theoretical background on the importance of AHF for UHI (Oke et al., 2017), the evidence of specific mechanisms linking selected types of human activities with various aspects of UHI is limited due to challenges in quantifying these associations. In mid-latitudes, AHF has a distinct seasonal pattern, and it has been considered a dominant contributor to UHI, especially during the cold part of the year. AHF is the product of human activities such as transportation, industrial and construction activities, heating, lighting, and human metabolism, and the heat flux is dissipated through both sensible and latent heat (Oke et al., 2017). The quantity and impact of these emission sources on UHI can significantly vary throughout a city, influenced by the intensity of human activities and the time of day. The amount of these emission sources and their impacts on UHI may vary significantly across a city, depending on the intensity of human activities and the time of day. For example, temporal dependence of UHI magnitude on the weekly commuting pattern has been documented in Australia (Earl et al., 2016), while another study observed a significant increase in UHI magnitude related to massive migration during the Lunar New Year celebrations in China (Zhang et al., 2015).

Although emissions of anthropogenic heat affect mainly the canopy UHI via enhanced sensible heat flux, SUHI is affected indirectly by modified thermal and radiative properties of the atmosphere (e.g., urban greenhouse effect) that intensifies the amount of heat emitted by the atmosphere back to the surface (Liu et al., 2021; Oke et al., 2017).

Therefore, studies have documented both long-term and short-term associations between SUHI magnitude and reduction in human activities (Alves et al., 2020; Firozjaei et al., 2020; Feng et al., 2021; Raj et al., 2020; Zhou et al., 2014). For example, a study in eastern China observed a positive correlation between SUHI magnitude and AHF (0.0275 °C warming of SUHI per each 1.0 W/m2 increase in AHF), which was estimated from energy consumption (Jin et al., 2020). Accordingly, prior research documented a significant association between SUHI and AHF in seven Chinese cities using a linear mixed-effect model (Qian et al., 2023).

Reduced mobility and transport of city dwellers have been considered to contribute an important part of the reduction in AHF during the COVID-19 lockdown (Liu et al., 2022; Wang and He, 2023). Data from Prague suggest an 80% drop in checked-in flights at the Prague airport and a 30% decrease in the city's traffic intensity (Letiště Praha, 2023; Ročenka dopravy Praha 2020, 2023). Accordingly, our results show a 29% and a 12% decrease in concentrations of NO2 and AOD, respectively, during Lockdown. Transportation data and our findings on air pollution support the hypothesis that the 0.1 °C (15%) decrease in mean daytime SUHI magnitude over urbanized areas in Prague and 0.7 °C decline in AUHI was driven by the decrease in AHF from human mobility during the lockdown period. The larger decrease in AUHI than in SUHI magnitude is in line with the indirect effect of AHF on SUHI. Similar to our findings, a larger reduction of daytime AUHI (by a mean of 0.42 K) than of SUHI (mean of 0.25 K) was observed during the COVID-19 lockdown in China (Liu et al., 2022).

Previous studies using the MODIS LST product to identify effects of the lockdown on SUHI revealed mean 0.20–0.41 K, 2 °C, and 0.25 K decreases in SUHI magnitude in the North Indian River Plain (Chakraborty et al., 2021), the Middle East (El Kenawy et al., 2021), and China (Liu et al., 2022), respectively. Most authors attribute these changes to reduced emissions of anthropogenic heat from traffic. For example, researchers documented a mean decrease in NO2, AOD, and SUHI, respectively, by 23.7%, 3.7%, and 19.2% in the United Arab Emirates during the lockdown compared to the same period in 2019 (Alqasemi et al., 2021). A study analyzing 43 European cities, on the other

hand, was not able to attribute the reduction of air pollution concentrations to mobility changes during the lockdown, due to large spatial variability dominated by meteorological patterns (Glocke et al., 2023).

When comparing the lockdown period to previous years, however, these studies considered the lockdown period as a whole, overlooking changes in synoptic conditions. A recent study also illustrated that nighttime LST in Paris and London were higher during the lockdown compared to 2019. However, this change was primarily driven by natural variability (due to higher temperatures during lockdown), and not related to changes in AHF (Safarrad et al., 2022). Similarly, some parts of Europe experienced an increase in LST from usual levels during the lockdown period (Parida et al., 2021). The authors hypothesized that this warming was related to anticyclonic weather conditions prevailing across a large part of Europe in spring 2020 and decreased concentrations of aerosols, which enhanced the amount of solar radiation incoming to the land surface. This could have enhanced the positive radiation balance during the lockdown period (Chakraborty et al., 2021; Chakraborty et al., 2023; Mazhar et al., 2021; Revathy et al., 2021). These findings highlight the important role of the natural variability of temperature and solar radiation that cannot be attributed to variations in AHF during lockdown. As far as we know, our study is the only one to analyze SUHI dynamics during the lockdown by rigorously selecting MODIS satellite images based on comparable synoptic conditions (i.e., taking into account similar temperature, cloud cover, and precipitation) and considering global radiation (as a proxy for solar radiation) (Appendix A). This approach ensured that our results would be more robust in the face of confounding factors.

In terms of spatial variability, our findings indicate a relatively small decrease in SUHI magnitude across the urbanized areas of Prague, while it even increased in some parts. While the decline in SUHI magnitude in urbanized areas was presumed to be linked to a decrease in AHF, this might not be the case in some historical parts of the city that have been within permanent traffic-restricted areas and/or pedestrian zones. In these areas, the changes in SUHI could be more influenced by favorable microclimatic conditions. Despite our efforts to mitigate the impact of

changes in synoptic conditions through a rigorous selection of satellite images and careful consideration of reference land cover types for SUHI calculation, we acknowledge the possibility of their effects on our results. On the other hand, the consistent spatial pattern of SUHI between the Reference and Lockdown periods, along with generally small differences observed between the two periods, underscore the robustness of our method. This highlights the importance of considering possible confounding factors when assessing the effect of lockdown on SUHI.

3.5.2 Role of Urban-Rural Dynamic

Most prior studies have either covered multiple regions or primarily concentrated on large-scale effects. Although some of the previous studies have acknowledged the effects of urban-rural dynamics when analyzing the changes in SUHI (Chakraborty et al., 2021), they often neglected the within-city dynamics between urban and rural land cover types when interpreting their results. Therefore, the options to compare our results with prior research are limited. For example, a 2°C decrease in SUHI was observed in Paris during lockdown (Safarrad et al., 2022). However, the spatial distribution of LST indicated a noteworthy temperature increase in surrounding rural areas, suggesting that a significant part of the SUHI decrease may have been attributable to increased LST in the rural areas. Given that the study did not consider the role of rural-urban dynamics or analyze the results in relation to development zones or urbanization, we are unable to compare its findings with ours. To better understand the role of urban-rural dynamics in the present study, we carefully distinguished urbanized and rural areas within the city boundaries when calculating the SUHI magnitude. Additionally, we investigated the complex interactions by employing the three concentric zones of Prague based on urbanization levels. As a result, we observed the largest decrease of SUHI magnitude in the Periphery zone with its predominantly rural land cover types. This is in line with some studies (Chakraborty et al., 2021; Mijani et al., 2023), although others have reported a larger LST decrease in urban areas compared to rural landscapes (Pal et al., 2021; Roshan et al., 2021; Mijani et al., 2023).

The additional analysis of SUHI changes in individual land cover classes

indicated a generally larger variance in SUHI magnitude for rural land cover types, especially arable land and forests (Figure A3), compared to urban land covers (Figure A3). The difference may arise from rural areas' natural systems and water reliance, which heighten their susceptibility to short-term and seasonal weather variations. These findings emphasize the importance of considering the effects of urban-rural dynamics within cities when attributing changes in SUHI magnitude to variations in AHF.

Although we tried to eliminate the effects of urban-rural dynamics on urbanized areas of Prague, results for the urban land cover classes were still affected by the "mixed pixels" problem (Peng et al., 2015). The pixel values of urban areas, particularly those that are small and adjacent to larger rural areas, may be influenced by the predominance of these surrounding rural areas. This is because each MODIS pixel also contains information from neighboring pixels (Peng et al., 2015). Hence, we may assume that SUHI variability in Inner City was predominantly driven by urban land cover characteristics and human-related activities, whereas changes in Periphery were primarily driven by the dynamics of prevalent rural land cover types, such as arable land and forests.

While previous studies provide knowledge and valuable insights, our study suggests that considering confounding factors such as changes in synoptic conditions and the urban-rural dynamics within city boundaries may provide better estimates and understanding of the effect of the COVID-19 lockdown on UHI and SUHI variations. Taking into account these factors, our findings support the hypothesis that the observed changes in SUHI magnitude within urbanized areas of the city were driven by the decrease in anthropogenic heat release during the lockdown period.

3.5.3 Limitations

We must acknowledge a few limitations of the study. First, due to lack of data on spatial distributions of anthropogenic heat sources and the amount of reduction in AHF during Lockdown, we were unable to solely attribute all changes to anthropogenic heat. Similarly, we could not quantify the specific impact of reduced AHF on the magnitude of SUHI. To estimate the effect of AHF reduction related to human activity, we

employed the three concentric zones of Prague that are based on the level of urbanization and population density. While our approach enhances understanding of potential effects of urban development and human activities, we recognize that a more comprehensive understanding could be achieved by incorporating data on anthropogenic heat sources.

In addition, as AHF depends on population density and economic activities in the city (Lindberg et al., 2013), it is highly variable among cities (Ahmed and Zan, 2022). This factor (together with methodological differences) limits meaningful comparison of our results with other case studies.

Furthermore, the study of SUHI changes relied on MODIS Aqua satellite images, which have inherent limitations. MODIS satellite images, while providing spatial coverage, may not capture the fine-scale variations in UHI effects within the city. For a more precise determination of the impact of human activities on urbanized areas in Prague, higher-resolution data (e.g., Landsat 8 images) could have been used to analyze the effects of the COVID-19 lockdown on SUHI (Cai et al., 2021; Sahani et al., 2020). Due to the low temporal resolution of Landsat, however, the number of available cloudless images was insufficient to be used in our methodology. Likewise, although nighttime UHI effects are generally more important in terms of health effects, we did not include nighttime analysis in this study due to high cloud coverage of the satellite images.

Another point of consideration is that air temperature data, while more precise and more relevant to human thermal comfort, are often restricted to a few stations. Thus, they do not fully capture the spatial variations in thermal conditions within a city. Therefore, many studies have utilized satellite images and remote sensing methods to analyze the spatial variations of UHIs in response to the COVID-19 lockdown (Wang and He, 2023).

Finally, although we implemented rigorous criteria to ensure comparable background conditions for the analyzed satellite images, we could not entirely eliminate the effects of synoptic variability on LST and urban-rural dynamics. Consequently, we could not quantify the specific

contribution of the lockdown to UHI changes. This is especially difficult during the spring season, which is characterized by large day-to-day weather variability in Central Europe (Scheifinger et al., 2002).

3.5.4 Future Research and Policy Implications

Controlling for potential confounding factors such as synoptic variability and urban-rural dynamics, our study suggests that the reduction of anthropogenic heat release can be used as an effective strategy to mitigate UHI effects in Prague, especially in the Inner City. Despite inconclusive results regarding SUHI and LST changes in Europe (Glocke et al., 2023; Parida et al., 2021), our results align with research indicating that reduced mobility during the COVID-19 lockdown considerably improved the air quality and AUHI conditions in the city. Additionally, employing a rigorous selection of satellite images to eliminate the differences in synoptic conditions, we observed a decrease in mean SUHI magnitude across the urbanized areas of Prague.

Our findings underscore the significant influence of urban-rural dynamics within a city on SUHI variability and the role of spatial dependence. We encourage follow-up studies to further eliminate these effects, thereby enabling a clearer understanding of the reduction of AHF's impact on SUHI. This approach aligns with Tobler's first law of geography, which emphasizes the importance of spatial dependence: "Everything is related to everything else, but near things are more related than distant things." (Tobler, 1970).

The literature suggests reduction in anthropogenic activities as a potential SUHI mitigation strategy (Alves et al., 2020; Feng et al., 2021; Firozjaei et al., 2020; Raj et al., 2020; Zhou et al., 2014) and our study emphasizes the importance of carefully considering the local context. Our findings indicate that, especially in the city's periphery, the effect of urban-rural dynamics needs to be taken into account when attributing changes in SUHI to anthropogenic activities. At the same time, mitigation strategies to reduce AHF in Periphery might not be as effective as anticipated due to the dominant influence of rural areas in this zone. A more sophisticated approach for quantifying the effect of urban-rural dynamics and investigating the relationship between spatial distribution of AHF and

SUHI magnitude should be considered in future research. Quantifying these effects is necessary to plan effective mitigation strategies (Qian et al., 2023).

With the emergence of the COVID-19 pandemic, many cities have implemented measures to promote and encourage active mobility (walking and cycling), as well as to revitalize urban areas. This includes increasing bike lanes, setting up low emission zones, limiting car traffic, and revitalizing parking lots (Wang and He, 2023). Beyond providing health benefits during the pandemic, these measures have other potential co-benefits such as improved air quality, reduced noise pollution, and reduced greenhouse gas emissions. Moreover, our study demonstrated that reduction in AHF during the lockdown as a result of transportation and industrial activities can reduce UHI and SUHI effects. Therefore, we recommend a transit-oriented development (TOD) approach that promotes sustainable, compact, and pedestrian-friendly urban design around transit hubs. TOD strategies, such as more green spaces, energy-efficient buildings, reduced car dependence, and fostering community engagement, enhance human health (improving air quality and thermal comfort), mitigate UHI, and promote urban resilience (Jacobson and Forsyth, 2008; Raya et al., 2022; Wey, 2015).

Overall, the experience with the COVID-19 pandemic and the results of subsequent studies can motivate urban climate researchers, city planners and policy makers to collaborate and develop more resilient cities (Wang and He, 2023).

3.4 Conclusion

The unprecedented social and economic stagnation experienced worldwide during the COVID-19 pandemic provided an opportunity to investigate the effect of AHF on UHI and SUHI. In this study, we employed a comprehensive analytical approach to assess effects of the COVID-19 lockdown on mean UHI, SUHI, and air quality distribution in Prague, Czechia. The Lockdown period during March–April 2020 was compared with the Reference period of March–April 2017–2019.

Our results show that, based on MODIS observation, the COVID-19 lockdown was associated with a 15% reduction in the daytime magnitude of SUHI in urbanized areas of Prague. These findings were consistent with the 0.7 °C increase in afternoon AUHI magnitude (considered as the difference between the city center station and reference station in the city outskirts). Likewise, two main air quality indicators based on satellite data, Aerosol Optical Depth and Offline Nitrogen Dioxide concentrations, showed a 12% and 29% decrease, respectively. Taking into account changes in synoptic conditions and the dynamics of LST in urban-rural dynamics, we hypothesize that these changes may be attributed to the decreased anthropogenic emissions, mainly through reduced transportation and industrial activities.

The method employed in the study, which eliminates the differences in synoptic conditions and enables comparison between different periods, can be used to understand the effect of changes in AHF on SUHI during lockdown in other cities.

Ultimately, our study not only provides important insights for scientists regarding anthropogenic heat effects on the SUHI phenomenon, but also incentives for public policymakers to understand the complex dynamics of urban heat islands, by highlighting the interplay between urban and rural microclimates.

Because UHI is a complex phenomenon influenced by various factors, successful mitigation strategies that enhance thermal comfort and air

quality can be achieved only through comprehensively understanding UHI. Such understanding can guide researchers and policymakers in developing targeted mitigation strategies that reduce the adverse effects of UHI on the environment and human well-being andalso promote sustainable urban development.

3.5. Appendix

Table A1. List of selected satellite images with dates, daily mean global radiation, and mean afternoon temperature (13:00–14:00 CET) as observed at Prague weather stations.

Weather station	Global radiation (kJ/m².).)		Air temperature (°C)			
	Karlov	Libus	Libus	Kbely	Karlov	Ruzyne
28 March 2017	18137	19551	21.6	21.5	22.5	21.0
31 March 2017	18060	19350	20.9	20.6	22.0	20.1
1 April 2017	18243	19518	18.7	19.1	19.2	19.2
7 April 2018	20936	21337	21.0	20.0	21.7	20.0
18 April 2018	22439	22908	22.4	22.5	23.8	21.9
19 April 2018	21669	22204	19.2	19.1	19.8	18.7
23 March 2019	17323	17570	20.9	20.6	21.2	20.3
19 April 2019	23617	24119	21.4	20.9	21.8	19.8
21 April 2019	23905	24517	20.4	19.2	20.8	19.1
22 April 2019	24333	25125	16.7	16.1	16.7	16.7
7 April 2020	20614	21511	20.0	19.1	20.7	18.7
8 April 2020	22022	22937	21.4	20.7	21.7	20.2
9 April 2020	20523	21371	21.3	20.9	21.8	20.3
12 April 2020	22195	23034	22.0	20.6	21.6	20.6
17 April 2020	22039	23039	21.1	19.4	20.7	19.8
22 April 2020	24899	25628	16.9	17.0	17.3	16.1
23 April 2020	24648	25472	19.2	18.4	19.1	18.2
27 April 2020	25154	24679	21.7	20.7	21.0	19.9
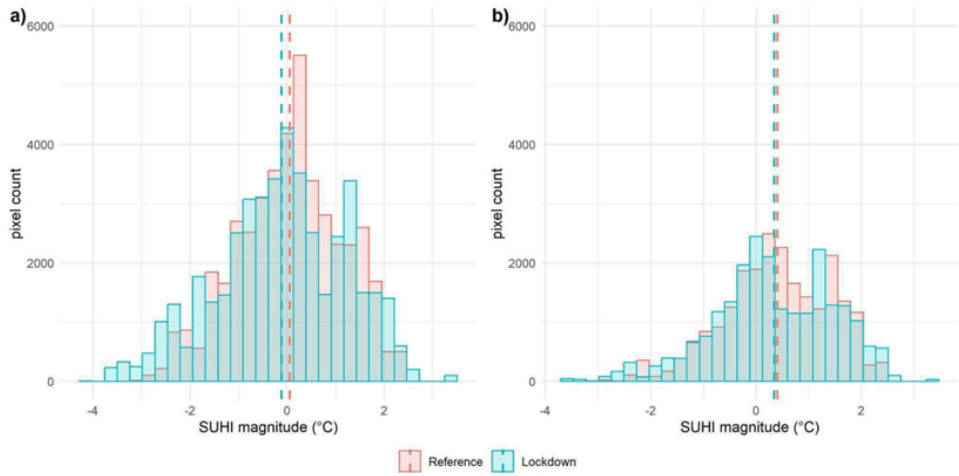
Figure A1. SUHI magnitude distribution in Prague in the Reference and Lockdown periods for a) the whole of Prague, and b) urbanized areas of Prague. Vertical broken lines indicate mean values for each period weighted by the numbers of pixels.
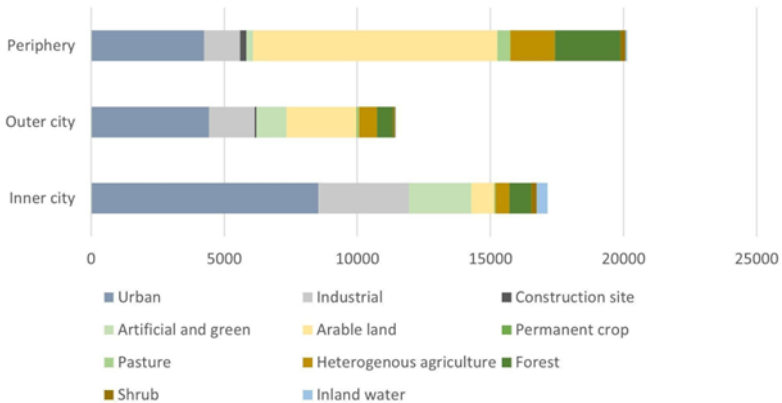
Figure A2. Land cover proportions in the zones within Prague.
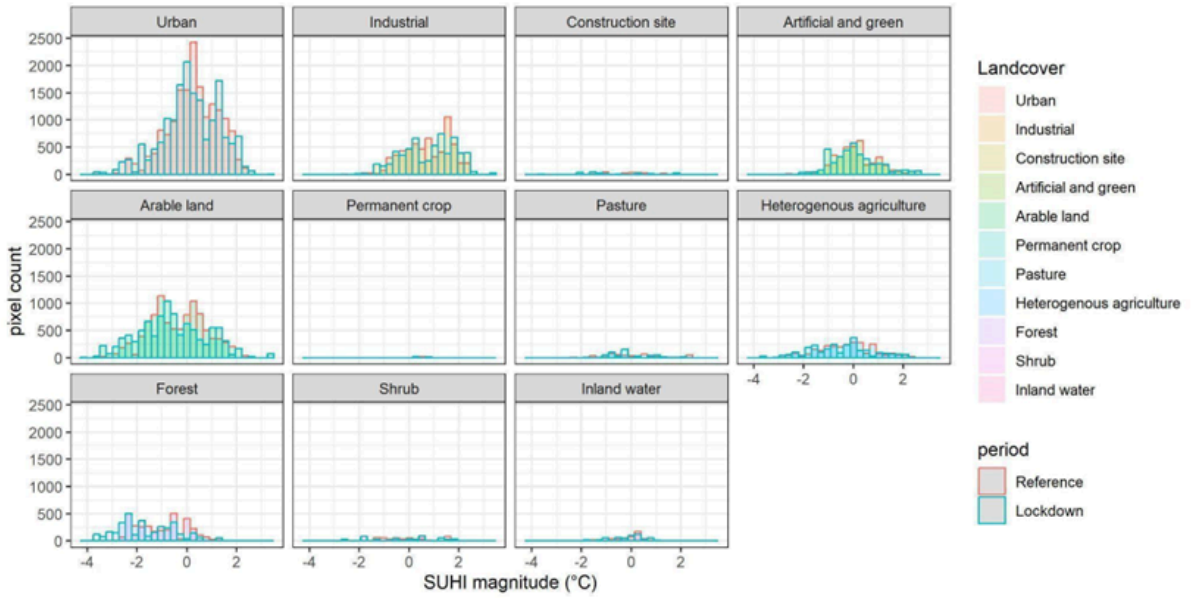
Figure A3. SUHI magnitude distribution (pixel count) for individual CORINE land cover classes in Prague for the Reference (Red outline) and Lockdown (Green outline) periods.

Chapter IV

Case Study III: Links between the spatial distribution of the land surface temperature and heat-related mortality in Prague, Czech Republic

Abstract

This study investigates the spatial distribution of land surface temperature (LST) and its association with heat-related mortality in seven zones of Prague, taking into account varying cloud cover conditions. We analyzed daily all-cause mortality in seven Prague districts between 2001 and 2020. Six major heat waves, defined as at least three consecutive days hotter than 95th percentile of daily mean temperature distribution over the study period, were selected to investigate the links between the spatial distribution of LST and heat-related mortality. Three selections of heatwave days (HWDs) were defined based on cloud coverage (less than 31%, 22%, and 14%) on the cloudiness amount. Daily MODIS land surface temperature images were used to analyze the spatial distribution in LST in the three selections of HWDs. Distributed lag non-linear models were used to quantify the relative risk (RR) of heat-related mortality on HWDs in the three selected groups. The results did not confirm spatial association between distribution of LST and heat-related mortality risk in Prague during major heat waves. On the contrary, the findings revealed a constituent distribution of districts with largest and lowest RR, suggesting that other than meteorological factors play a significant role. On the other hand, the analysis showed that HWDs with smaller cloudiness were associated with higher Relative Risk (RR) of mortality values despite lower LST. These findings indicate that hot summer days with minimum cloudiness represent a higher threat for human health than their cloudy counterparts.

4.1 Introduction

Episodes of extremely high temperatures, heatwaves, are associated with an increased risk of human mortality (Gosling et al., 2009). Due to climate change occurrence, duration and intensity of heat waves (HWs) is very likely to increase (Lhotka, Kyselý, and Farda, 2017). Researchers analyzed real-world data from 732 sites in 43 countries to determine the mortality burdens related to the increased heat exposure caused by recent anthropogenic global warming from 1991 to 2018. It was found that 37.0% (ranging from 20.5–76.3%) of heat-related deaths during the warm seasons in all the countries studied were attributable to human-induced climate change (Vicedo-Cabrera et al., 2021). Extreme temperature events disproportionately impact vulnerable populations, exacerbating health inequalities within and across nations (Green et al., 2019; Gronlund, Zanobetti, Wellenius, Schwartz, and O'Neill, 2016).

People living in cities are at the most significant risk of heat-related mortality due to the urban heat island effect (Oke et al. 2017). The 2003 European heat wave led to over 20,000 deaths, with a peak temperature of 73°C in the first two weeks of August (Fennessy and Kinter, 2011). Moreover, research suggested that the UHI contributed around 50 % of the total heat-related mortality during the 2003 heatwave in the West Midlands (Heaviside, Vardoulakis, and Cai, 2016). A study on northeastern Germany showed that, throughout the heat waves from 1990 to 2006, health risks were more pronounced for the elderly in both countryside and city regions (Gabriel and Endlicher, 2011). However, during the two primary heat waves in that 17-year span, the city of Berlin, especially its most densely populated areas, recorded the highest

mortality rates (Gabriel and Endlicher, 2011).

HWs can significantly influence the spatial and temporal fluctuations of UHIs by modifying the transfer of sensible and latent heat, as well as by shifting wind patterns (Li et al., 2015; Li, Sun, Liu, Wang, and Gao, 2016). A study showed that during heatwave, the severity of the UHI increased by about 4°C in Mashhad and Ahvaz, 6°C in Tabriz, and 3°C in Tehran, compared to the days when there was no heatwave (Keikhosravi, 2019). Similarly, in Cluj-Napoca intensity and extent of UHI are found to be controlled by heatwaves (Herbel et al., 2017). Therefore, it is necessary for a more comprehensive and interconnected examination of UHI, which incorporates aspects such as heatwaves in urban areas and global climate change in forthcoming research (Santamouris, 2020).

Prior studies have demonstrated that mitigating UHIs can prevent heat-related mortality (Burkart et al., 2016). This can be achieved by reducing temperatures in micro-urban heat islands, which may lessen the health impact of high temperatures and potentially decrease daily mortality rates during warm summer days (Smargiassi et al., 2009). Furthermore, during heat wave periods in the Greater Montreal Area, Canada, it was discovered that enhancing surface reflectivity in UHIs could reduce heat-related mortality by nearly 3.2% (Jandaghian and Akbari, 2018). Additionally, by modifying vegetation and surface albedo in US cities, there is potential to counteract projected increases in heat-related mortality by 40 to 99% by 2050 (Stone et al., 2014).

However, UHI research is constrained by the availability of data, resulting in limited information for devising effective mitigation strategies. Usually, temperature observation points are located outside urban cores. This placement can lead to a discrepancy between the recorded temperatures and the actual temperatures within city centres. Consequently, health impact assessments based on these measurements might underestimate the effects of heat on public health. Therefore, SUHI analysis is employed to examine the intra-city variation of Land Surface Temperature (LST) and estimate potential health impacts within the city.

Using Sentinel-3A and 3B imagery, researchers explored interactions between LST, Surface SUHI, and heatwaves in Andalusia's eight capital

cities during July and August of 2019 and 2020 (García, 2021). The findings reveal that LST and mean SUHI are statistically linked and intensify during heat waves. Coastal cities experienced the greatest daytime temperature increases with Sentinel-3A (LST = 3.90 °C, SUHI = 1.44 °C), while inland cities saw similar effects with Sentinel-3B (LST = 2.85 °C, SUHI = 0.52 °C) (García, 2021).

There is a need for more comprehensive and integrated studies that can address the research gaps and challenges in UHI and heat-related mortality research, such as the spatial and temporal variations in SUHII and mortality, the factors that influence the vulnerability and adaptation of different populations, and the potential impacts of climate change and urbanization on these phenomena. Although most studies investigate the impact of heat stress on mortality in a city as a whole, the magnitude of the heat stress in a particular part of the city depends on its physical characteristics.

The aim of this study is to investigate links between the spatial distribution of LST and heat-related mortality in Prague, the Czech Republic. Our study hypothesizes that the spatial distribution of heat-related mortality is associated with the distribution of SUHII during the major heat waves. The results of our study will help to identify zones in Prague with the most significant impact of urban design on heat-related mortality. This information is vital for identifying hot spots of heat-related mortality and developing strategies to mitigate heat stress in the city.

4.2 Materials and Methods

4.2.1 Data

Daily all-caused mortality data in 22 Prague districts (Figure 4.1), covering the period 2010–2020, were provided by the Czech Statistical Office for the purpose of the analysis. Due to the low number of cases in some districts that did not allow for robust results, the 22 administrative districts were aggregated to seven larger areas (Figure 4.1).

Daily mean temperature data averaged from Prague four weather stations operated by the Czech Hydrometeorological Institute (Praha-Ruzyně, Praha-Karlov, Praha-Libuš, and Praha-Kbely) were used as a proxy variable of the ambient thermal conditions. Additionally, daily land surface temperature data from the Moderate Resolution Imaging Spectroradiometer (MODIS) sensor onboard Aqua satellites, covering the period from 2001 to 2020 were used to analyze the spatial patterns in surface urban heat island.

Figure 4.1. Administrative districts of Prague (Geoportal Prague 2020).

Figure 4.2. The merged ten zones of Prague.

4.3 Methods

The study design followed the workflow (illustrated in Figure 4.3) divided into three main stages: In the first stage, based on the air temperature data, major heat wave periods occuring in Prague during the period 2010–2020 were defined as at least three consecutive days with a mean daily temperature higher than the 95th percentile of the summer (June-August) temperature distribution across the whole study period. Days meeting the heatwave definition were defined as heatwave days (HWDs).

Figure 4.3. The workflow of the study.

In the second stage, selected HWDs were checked for meteorological conditions other than temperature (i.e. cloud cover and precipitation) in order to select days suitable for the analysis of LST from satellite images. Three different selections of HWDs, based on different cloud cover thresholds were defined. Consequently, LST was derived from MODIS images on days that met the selection criteria.
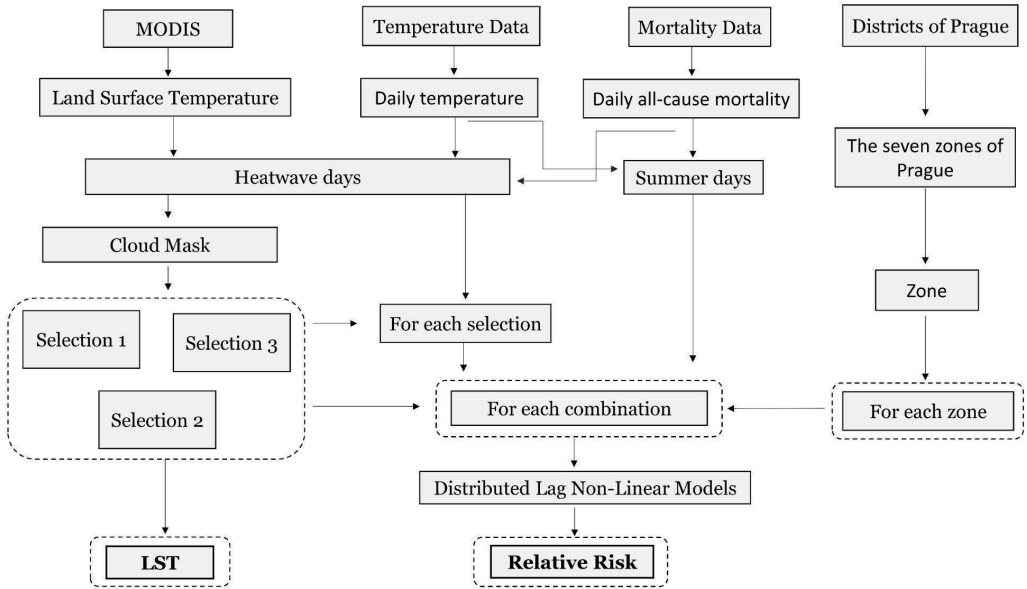
In the third stage, Distributed Lag Non-Linear models (DLNMs) were employed to quantify the relative risk of mortality on HWDs falling into the three selection groups, compared to the remaining days in the summer season in each of the 7 Prague zones, therefore in total the method was applied twenty one times (seven ones for three selections). More details on the individual stages are provided below.

4.3.1 Land surface temperature

To analyze spatial distribution of LST, MODIS images that are acquired by Aqua satellite with 1 km spatial resolution were used. The image acquisition time is around 13.30, therefore suitable for the aim of the study. LST maps derived via the Google Earth Engine. To further overcome the limitation of cloudiness and also understand their role,

images/days with more than 30% cloudiness were excluded; the remaining 23 images were divided into three groups (Selection 1, 2, and 3 as described in Figure 4.4) . For each selection, median LST was calculated. Zonal statistics tool in ArcGIS was used to investigate the spatio-temporal patterns.

	Date	Prague	Prague 1	Prague 4	Prague 5	Prague 6	Prague 8	Prague 9	Prague 10
					Cloud Cover Percentage %				
Selection 1		< 31 %				< 47 %			
	July 26, 2013	30	0	36	41	38	21	36	10
	July 19, 2014	30	23	39	29	9	17	46	23
	June 25, 2016	29	5	16	42	21	20	36	33
	August 12, 2015	25	5	10	34	31	17	31	23
	July 25, 2006	24	0	15	34	8	17	43	11
	July 18, 2014	23	0	26	34	13	6	25	23
	August 14, 2015	20	0	24	15	25	44	17	12
Selection 2		< 22 %				< 37 %			
	July 17, 2007	21	21	16	17	34	17	21	24
	July 27, 2012	21	0	19	34	6	25	25	11
	July 20, 2014	19	0	14	33	20	7	15	23
	July 12, 2010	18	0	35	34	23	2	0	12
	August 10, 2015	17	13	17	9	28	23	15	22
	July 14, 2010	14	0	10	12	6	31	9	28
	August 8, 2020	14	0	1	2	12	4	36	24
Selection 3		< 14 %				< 29 %			
	August 3, 2003	13	0	10	12	0	3	19	24
	July 29, 2018	12	0	3	17	15	27	15	4
	August 11, 2015	11	0	19	10	0	16	0	26
	June 18, 2013	11	0	3	5	21	12	5	28
	August 5, 2015	8	3	9	4	2	4	13	10
	July 26, 2012	8	0	3	13	7	0	12	7
	July 31, 2017	7	0	17	2	19	6	5	3
	August 23, 2011	2	0	0	4	7	2	3	0
	August 4, 2015	1	0	0	4	0	0	1	3

Figure 4.4. The three selections and cloud cover percentages of the seven zones.

4.3.2 Heat-related mortality risk estimate

Generalized Additive Models (GAMs, Wood 2006) that follows a quasi-Poisson distribution, were applied to adjust mortality time series in each district for long-term trends and seasonal fluctuations (REF). Consequently, distributed lag nonlinear models (DLNM, Gassparini et al. 2010) were employed to quantify relative risk (RR) of mortality on the selected HWDs in each Prague zone. RR expresses the ratio of the likelihood of death in the exposed population compared to the unexposed population. DLNM is a class of models introduced by Gasaprrini et al.

(2010) to consider the lagged effects of exposure variables on health variables. This is achieved via a cross-basis matrix introduced into the Poisson regression model that enables modeling non-linear effects of exposure variables while taking into account their lag.

The Poisson family of time series regression models is commonly employed for the analysis of count variables, such as the number of deaths. These variables typically exhibit discrete positive values, and their variance is equal to their mean (REF). The Quasi-Poisson family offers a more flexible approach by allowing the variance to be proportional to the expected value. This flexibility is particularly useful when analyzing overdispersed data, i.e. where the variance exceeds the mean. Such overdispersion is frequently observed in mortality data, especially within populations with a small number of daily cases. (Quasi-)Poisson models are fitted by a logarithmic function. This means that coefficients in the models are expressed on a logarithmic scale, providing a logarithmic transformation of the expected count. Therefore, exponential values of the coefficients need to be calculated to get the real effect.

The specific model developed in this study can be outlined as follows:

$$\{log(\mu_t) = \alpha + cb + DOW_t + ns(DOY_{t'}, df = 2): factor(year_t)$$

$$+ ns(time, df = 1 \, per \, decade)$$

$$\mu_t = E(Y_t)$$

where Y_t is expected count of deaths, t is the expected value on a logarithmic scale, represents the intercept, cb is the cross-basis matrix, DOW stands for a categorical variable of the day-of-the-week (1 to 7), DOY represents the day-of-the-year and s stands for a smoothing spline to model non-linear effects of DOY and time. Flexibility of a smoothing spline is defined by the number of degrees of freedom (df). Two degrees of freedom are used to adjust for mortality variation within the summer season (Ellena et al. 2020). The time variable is used to adjust the model for long term changes in overall mortality rates due to demographic and socioeconomic factors. Analogically to previous studies (Achebak et al. 2018), a smoothing spline with one degree of freedom per decade was

used.

In the context of this study, the impact of heat on mortality was represented by a cross-basis (cb), which estimated the effect of HWDs while taking into account the lagged effect of heat (Sheridan and Dixon 2017). HWD was defined as a binary variable (0 or 1) where 1 stands for HWD. The lag-mortality effect was captured by a natural cubic spline with two internal knots evenly distributed on the logarithmic scale. The lag duration was prolonged to 10 days (following Sheridan and Dixon 2017).

The primary outcome of (quasi-) Poisson regression models are the regression coefficients of the variables being modeled, where their exponents correspond to the relative risk (RR) of mortality. In this case study, the coefficients of the exposure variable (HWD), represent the RR of mortality as a ratio between the likelihood of a mortality at a specific exposure (HWD = 1) and the likelihood of a mortality at a reference exposure (HWD = 0), considering the delayed effects. Figure X shows an example of the HWD effect in Prague 1 for Selection 1. While Figure X (left) suggests that there is a significantly increased risk of mortality up to lag 4 after the HWD onset (with maximum RR = 1.1 on lag 0), Figure X (right) shows the overall effect of HWDs up to lag 10 (RR=1.5).
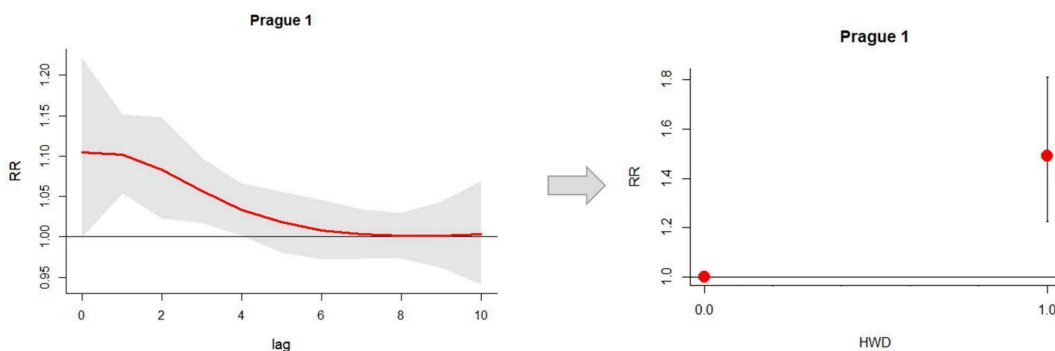

Figure 4.5. Left: lag-response effect of heatwave days (HWD) on the relative risk (RR) of mortality on days (lag) 0 to 10 after the HWD onset in Prague 1 in Selection 1. Right: Overall RR of mortality on HWDs, considering the lagged effect.

Overall Relative Risks of mortality on HWDs, considering a lagged effect up to 10 days, were calculated for the three selections and each Prague

zone separately. All modeling and computations were carried out using mgcv (version 1.8-42) and dlnm packages (version 2.4.7) in the software R (version 4.1.2).

4.4. Results and Discussions

In this study, we analyzed the spatial distribution of LST and heatwave-related mortality across seven zones in Prague to understand their relationship. We divided our data into three selections based on cloud coverage to also examine the impact of cloud cover on this association. The 19 time series that depict mortality rates from 2001 to 2020 across seven districts in Prague have been modeled using DLNMs with a quasi-Poisson family distribution, as outlined in the methods. For each district, the RR was calculated for the chosen HWDs in relation to summer temperatures and lags ranging from 1 to 10 days.

In Selection 1 , comprising 23 images with cloud cover less than 31%, the RR values for districts 1, 4, 5, 6, 8, 9, and 10 were 1.9, 2.3, 1.7, 1.5, 1.6, 1.1, and 2 respectively. Correspondingly, the mean LST values ranged from 35.6 to 38.4, providing a baseline understanding of the temperature-mortality association under moderate cloud cover.
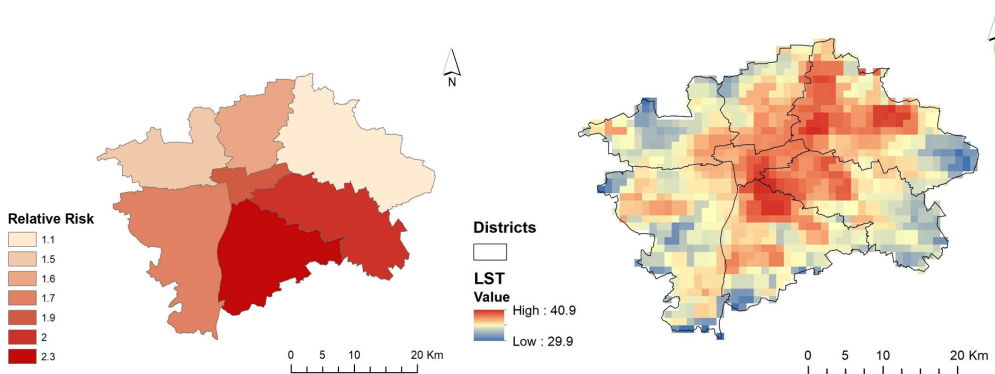

Figure 4.6. Relative Risk values of the seven districts and LST comparison based on Selection 1.

In the second selection, which included 16 images with cloud cover less than 22%, we observed an escalation in RR values across the same districts. Notably, districts 1, 4, and 10 exhibited higher RR values of 2.7,

3.7, and 3.3, indicating an augmented risk of heat-related mortality in clearer sky conditions. The associated LST values ranged from 35.8 to 38.2, reinforcing the impact of reduced cloud cover on elevated temperatures and subsequent health risks.
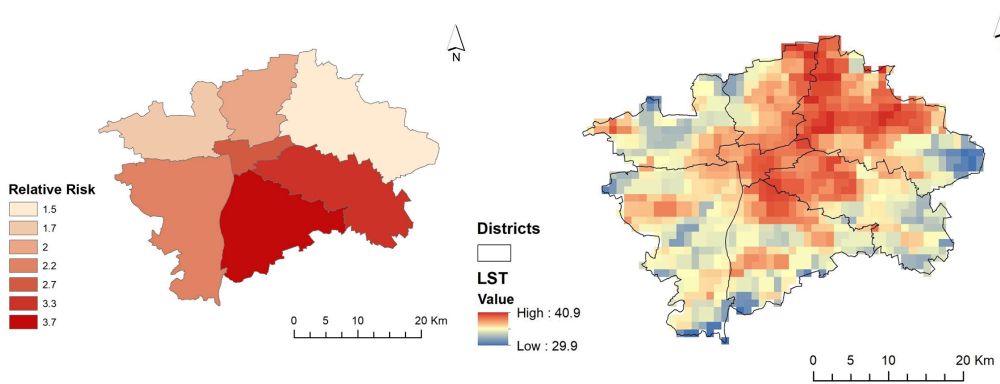

Figure 4.7. Relative Risk values of the seven districts and LST comparison based on Selection 2.

In the Selection 3, consisting of 9 images with cloud cover less than 14%, the RR values surged dramatically across all districts. District 1, for instance, demonstrated a striking RR value of 9.2, emphasizing an unprecedented susceptibility to heat-related mortality in extremely clear atmospheric conditions. The corresponding LST values ranged from 35.1 to 37.0, highlighting the substantial influence of diminished cloud cover on temperature extremes and the resultant health implications.
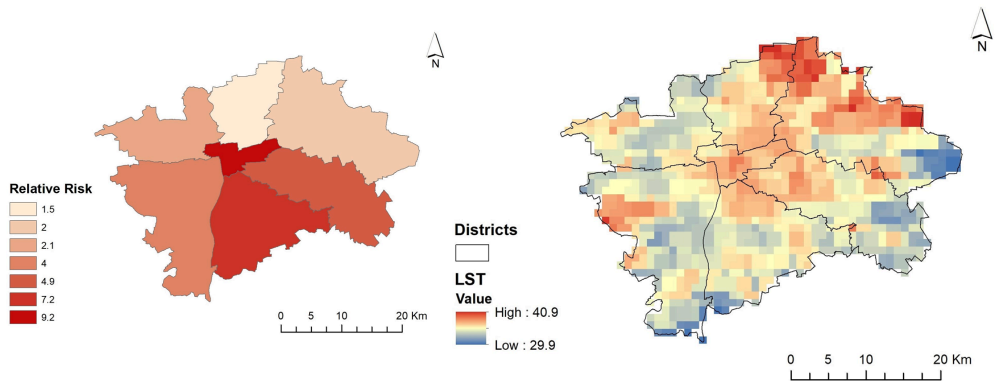

Figure 4.8. Relative Risk values of the seven districts and LST comparison based on Selection 3.

Districts 1, 4 and 10 consistently exhibit higher RR values across all three selections. District 1, in particular, displays a notable escalation from 1.9

to 2.7 and further to 9.2 as cloud cover decreases. This indicates a persistent and heightened vulnerability to heat related mortality in these districts, influenced by urban heat island effects. The substantial changes in RR values with varying cloud cover indicate a strong association between reduced cloud cover on hot summer days and increased health risks. These districts may be particularly sensitive to atmospheric conditions, requiring targeted interventions during periods of clearer skies.
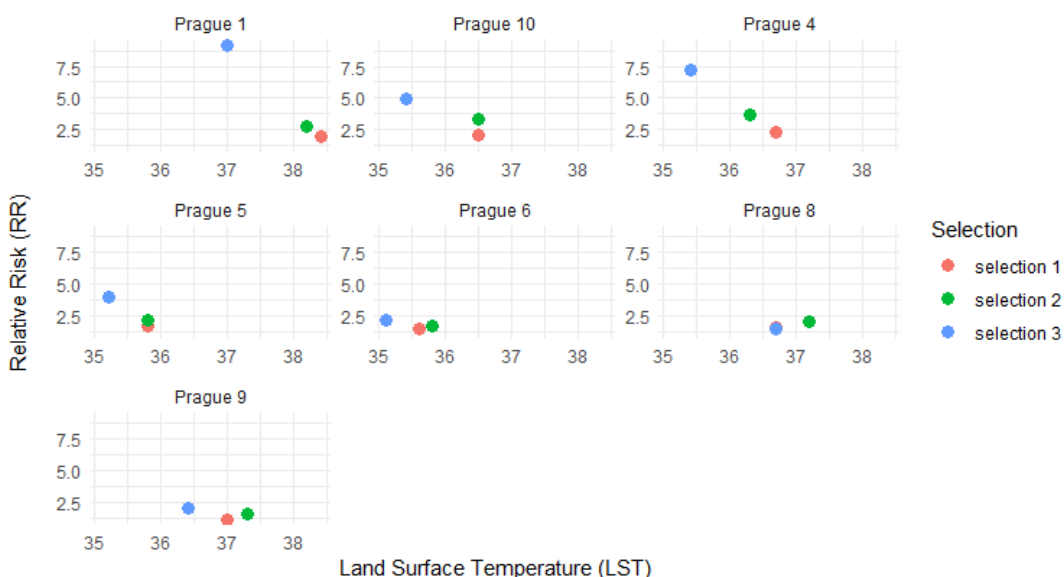
Figure 4.9. The relationship between LST and RR in different zones and selections.

On the other hand, districts 6, 8 and 9 show moderate to lower RR values in Selection 1, with fluctuations in subsequent selections. District 6, for example, has RR values of 1.5, 1.7, and 2.1 across Selections 1, 2, and 3, respectively. These districts show more moderate changes in RR values with decreasing cloud cover. While still influenced by atmospheric conditions, other factors may contribute to their overall vulnerability and comprehensive risk assessments are needed for a better understanding of local factors contributing to health risks.

District 5 displays an interesting pattern, with RR values increasing from 1.7 to 2.2 and further to 4.0 across the selections. This district's

vulnerability to heat-related mortality RR appears to amplify with decreasing cloud cover, emphasizing the importance of considering atmospheric conditions in risk assessments.

Overall, there is spatial variability in LST across the seven districts, even within the same cloud cover selection. Districts 1 and 10 consistently experience higher temperatures, suggesting potential urban heat island effects or local climate patterns influencing temperature distributions. Moreover, local climate patterns, including wind circulation and topography, may contribute to the observed spatial differences in temperature and heat-related mortality. Although the LST maps are a convenient tool for identifying hot spots, they only partially explain the spatial distribution of heat-related mortality. Therefore other factors need to be considered when implementing measures to reduce heat-related mortality risk. For example, variability in socio-economic conditions across districts that influences vulnerability and adaptive capacities to extreme temperatures may also play a role.

The observed relationship between LST and heat-related mortality risk appears to be influenced by cloud cover which indicates higher. Lower cloud cover intensifies the association, emphasizing the mediating role of atmospheric conditions in modifying health risks. The images with less cloud coverage explain better the spatial distribution of heat-related mortality. Therefore similar studies should be taken into account while selecting images. This highlights the need to consider meteorological factors in epidemiological studies to enhance the precision of risk assessments.

The results indicate that the risk of heat-related mortality and the mean LST vary across the different zones and selections. As cloud cover decreases from Selections 1 to Selections to Selections 3, the RR values generally increase across all districts. Higher RR values in lower cloud cover selections may suggest a stronger association between LST and heat-related mortality due to increased heat exposure. There is a notable trend of increasing RR values as cloud cover decreases in all seven zones. This suggests a stronger association between LST and heat-related mortality when skies are clearer. Higher RR values in lower cloud cover

selections may suggest a higher heat-related mortality risk due to increased heat exposure.

LST, on the other hand, varies across districts and selections but does not show a consistent pattern with cloud cover percentages. This suggests that higher temperatures, associated with lower cloud cover, increase the risk of heat-related mortality, while between LST and mortality is rather indirect. Additionally, spatial distribution of heat wave-related mortality within the city may vary with factors such as demographic characteristics, socioeconomic factors, and health infrastructure. Further research is needed to fully understand these spatial relationships on the microscale level and to develop effective public health strategies to mitigate the impact of heatwaves.

4.5 Conclusions

The main findings of this study did not confirm spatial association of heat-related mortality in Prague with LST during the major heat waves. On the other hand, comparison of the three groups of HWDs selected based on the cloud cover amount revealed that HWDs with smaller cloudiness were associated with higher Relative Risk (RR) of mortality despite lower LST. These findings indicate that hot summer days with minimum cloudiness represent a higher threat for human health than their cloudy counterparts.

Particularly, districts 1, 4, and 10 consistently show higher RR values, suggesting a greater susceptibility to heat exposure. These districts, therefore, may require targeted public health interventions and adaptive measures due to their heightened sensitivity to temperature extremes.

The variability in RR and LST across districts could be attributed to differences in SUHI effects, socio-economic factors, and local climate patterns. This underlines the importance of tailored urban planning

strategies. For instance, measures such as increasing green spaces or optimizing building design could be particularly effective in these high-risk districts.

The study also highlights the mediating effect of cloud cover, emphasizing the need to consider atmospheric conditions when assessing health risks associated with extreme temperatures. Further research should consider this effect to not to underestimate the RR and image with low cloud cover needs to be used to analyze heat related mortality.

Moreover, urban planning strategies aimed at mitigating heat island effects in vulnerable districts could be instrumental in reducing heat-related health risks. The findings of this study could help identify areas in Prague with the highest impact on human health, where mitigation measures should be targeted.

The study acknowledges the complex nature of LST and heat-related mortality, and the uncertainties in terms of issues and approaches on implementation. It calls for an integrated approach combining urban planning, public health policies, and climate change strategies to reduce heat intensity, mortality risks, and enhance urban resilience, especially for vulnerable groups. Future research opportunities lie in utilizing comprehensive data, incorporating relevant variables, comparing different measures and models, and developing effective interventions for urban heat issues.

Chapter V

5. Conclusions

This thesis examined the SUHI phenomenon through three case studies, each focusing on different aspects. It investigated how land cover changes, reduction in anthropogenic heat during COVID-19 lockdown, and human health are connected to SUHI formation. Each case study reveals different limitations of studying SUHI, demonstrating the importance of multi facade perspectives to deeply understand the topic.

Case Study I examined the impact of land cover changes on the development of SUHI in Prague, and revealed that the main increase was due to the conversion of agricultural areas into urban areas. Notably, these changes were more significant in areas 9 km to 12 km away from the city center, suggesting that peri-urbanization has intensified SUHI in Prague. The study emphasized the need for urban planning to consider these land cover changes and promote green infrastructure and sustainable strategies.

Case Study II explored the effect of anthropogenic heat on SUHI utilizing the unique real-life experimental situation COVID-19 lockdown provided. A comparison of the lockdown period with a reference period revealed a 15% reduction in SUHI in Prague's urbanized areas, potentially due to decreased anthropogenic emissions. This highlights the often overlooked role of anthropogenic heat on mitigation of UHI and SUHI. Although these changes were during the cooler months of March and April, provide valuable insights into the potential benefits of reduced anthropogenic heat's potential of mitigating UHI effects

Case study III anaylzed the links between LST and heat-related mortality in Prague. Finally, although the study did not confirm spatial association of heat-related mortality in Prague with LST during the major heat waves, comparison of the three groups of HWDs selected based on the cloud cover amount revealed that HWDs with smaller cloudiness were associated with higher Relative Risk (RR) of mortality despite lower LST. These findings indicate that hot summer days with minimum cloudiness represent a higher threat for human health than their cloudy counterparts. Additionally, the results highlighted the increased vulnerability to extreme temperatures in Prague districts 1, 4, and 10, and the need for targeted public health interventions. The study emphasized the importance of tailored urban planning strategies to mitigate heat island effects in vulnerable districts, considering the variability in RR and LST across districts can not be explained only by SUHI effects and other factors that need to be investigated such as by socio-economic factors, and local climate patterns. This study provides valuable insights into the relationship between heatwaves and the intensification of the urban heat island effect, which has significant implications for urban planning and public health in the context of climate change.

In summary, these case studies collectively highlight the complex relationship between urbanization, land cover changes, anthropogenic heat flux, and heat-related mortality in shaping the UHI and SUHI effects in Prague. They highlight the importance of integrated and sustainable urban planning strategies that consider these complex interactions to enhance urban resilience, reduce heat intensity and mortality risks, and improve thermal comfort and air quality. Future research should aim to utilize high-resolution regional climate models to investigate the UHI and SUHI dynamics under climate conditions to direct targeted mitigation strategies.

The findings of this thesis not only contribute to the academic discourse surrounding urban climatology but also hold practical implications for policymakers, urban planners, and public health officials. As we navigate the complexities of contemporary urban environments, the insights garnered from this research provide a valuable foundation for informed decision-making and sustainable urban development.

5.1. Further Research

Given the findings of this thesis, there are several promising directions for future research:

- Deepening the Understanding of Land Cover Changes: The first case study highlighted the impact of land cover changes, particularly the conversion of agricultural areas into urban areas, on SUHI. Future research could delve deeper into this area, investigating the specific types of urban development (e.g., residential, commercial, industrial) that contribute most to SUHI. Additionally, studies could explore the impact of different types of green infrastructure on mitigating SUHI.

- Anthropogenic Heat and SUHI: The second case study underscored the role of anthropogenic heat in SUHI. Future research could extend this investigation to other cities and different seasons, providing a more comprehensive understanding of how anthropogenic heat influences SUHI. Moreover, studies could explore the potential of various strategies for reducing anthropogenic heat, such as energy-efficient buildings and transportation systems.

- Heat-Related Mortality and SUHI: The third case study revealed the complex relationship between heat-related mortality, cloud cover, and SUHI. Future research could further investigate this relationship, considering other potential factors such as air pollution, humidity, and wind speed. Additionally, studies could examine the effectiveness of public health interventions in reducing heat-related mortality.

- High-Resolution Regional Climate Models: The thesis suggests the use of high-resolution regional climate models to investigate UHI and SUHI dynamics under future climate conditions. This could be a fruitful area for future research, helping to predict future trends and inform mitigation strategies.

- Socio-Economic Factors and SUHI: The thesis also highlighted the need to consider socio-economic factors in understanding and addressing SUHI. Future research could explore this in more detail, examining how factors such as income, education, and access to healthcare influence vulnerability to SUHI.

● Policy and Planning Implications: Finally, future research could focus on the policy and planning implications of these findings, exploring how they can be translated into effective strategies for sustainable urban development. This could involve collaboration with policymakers, urban planners, and public health officials, ensuring that research findings are effectively applied in practice.

In summary, while this thesis has made significant contributions to our understanding of SUHI, there is still much to learn. Future research in these areas could provide valuable insights, helping to enhance urban resilience, reduce heat intensity and mortality risks, and improve thermal comfort and air quality.

Chapter VI

References

Achebak, H., D. Devolder, and J. Ballester (2018). Heat-Related Mortality Trends under Recent Climate Warming in Spain: A 36-Year Observational Study. *Plos Med* 15.7, e1002617. doi: 10.1371/journal.pmed.1002617

Aguiar, A. (2012). Urban Heat Islands: differentiating between the benefits and drawbacks of using native or exotic vegetation in mitigating climate. (Master). University of Wollongong.

Ahmed, G., and Zan, M. (2022). Impact of COVID-19 Restrictions on Air Quality and Surface Urban Heat Island Effect within the Main Urban Area of Urumqi, China. *Environmental Science and Pollution Research*, 30(6), 16333–16345. https://doi.org/10.1007/s11356-022-23159-6.

Alqasemi, A. S., Hereher, M. E., Kaplan, G., Al-Quraishi, A. M. F., and Saibi, H. (2021). Impact of COVID-19 Lockdown upon the Air Quality and Surface Urban Heat Island Intensity over the United Arab Emirates. *Science of The Total Environment*, 767, 144330. https://doi.org/10.1016/j.scitotenv.2020.144330.

Alves, E., Anjos, M., and Galvani, E. (2020). Surface Urban Heat Island in Middle City: Spatial and Temporal Characteristics. *Urban Science*, 4(4), 54. https://doi.org/10.3390/urbansci4040054.

Anderson, B. G. and M. L. Bell (2009). Weather-Related Mortality: How Heat, Cold, and Heat Waves Affect Mortality in the United States. *Epidemiology* 20.2, pp. 205–213. doi: 10.1097/EDE.0b013e318190ee08.

Argaud, L., Ferry, T., Le, Q.-H., Marfisi, A., Ciorba, D., Achache, P., Ducluzeau, R., Robert, D. (2007). Short- and long-term outcomes of heatstroke following the 2003 heat wave in Lyon, France. *Archives of Internal Medicine*, 167(20), 2177–2183.

Arnfield, A.J. (2003) 'Two decades of urban climate research: A review of turbulence, exchanges of energy and water, and the urban heat island', *International Journal of Climatology*, 23(1), pp. 1–26. doi: 10.1002/joc.859.

Avdan, U., & Jovanovska, G. (2016). Algorithm for Automated Mapping of Land Surface Temperature Using LANDSAT 8 Satellite Data. Journal of Sensors, 2016, 1–8. https://doi.org/10.1155/2016/1480307

Bokaie, M., Zarkesh, M., Arasteh, P. and Hosseini, A. (2016). Assessment of Urban Heat Island based on the relationship between land surface temperature and Land Use/ Land Cover in Tehran. *Sustainable Cities and Society*, 23, pp.94-104.

Burkart, K., Meier, F., Schneider, A., Breitner, S., Canário, P., Alcoforado, M. J., . . . Endlicher, W. (2016). Modification of Heat-Related Mortality in an Elderly Urban Population by Vegetation (Urban Green) and Proximity to Water (Urban Blue): Evidence from Lisbon, Portugal. *Environmental Health Perspectives*, 124(7), 927–934. https://doi.org/10.1289/ehp.1409529

Cai, Z., Tang, Y., and Zhan, Q. (2021). A Cooled City? Comparing Human Activity Changes on the Impact of Urban Thermal Environment before and after City-Wide Lockdown. *Building and Environment*, 195, 107729. https://doi.org/10.1016/j.buildenv.2021.107729.

Chakraborty, T., Das, D., Hamdi, R., Khan, A., and Niyogi, D. (2023). Large-Scale Urban Heating and Pollution Domes over the Indian Subcontinent. *Remote Sensing*, 15(10), 2681. https://doi.org/10.3390/rs15102681.

Chakraborty, T., Sarangi, C., and Lee, X. (2021). Reduction in Human Activity Can Enhance the Urban Heat Island: Insights from the COVID-19 Lockdown. *Environmental Research Letters*, 16(5), 054060. https://doi.org/10.1088/1748-9326/abef8e.

Chen, S., and Hu, D. (2017). Parameterizing Anthropogenic Heat Flux with an Energy-Consumption Inventory and Multi-Source Remote Sensing Data. *Remote Sensing*, 9(11), 1165. https://doi.org/10.3390/rs9111165.

Chen, X., Zhao, H., Li, P. and Yin, Z. (2006). Remote sensing image-based analysis of the relationship between urban heat island and land use/cover changes. *Remote Sensing of Environment*, 104(2), pp.133-146.

CORINE Land Cover. Available at: https://land.copernicus.eu/en/products/corine-land-cover (accessed January 10, 2023).

Dixon, P., and Mote, T. (2003). Patterns and Causes of Atlanta's Urban Heat Island–Initiated Precipitation. *Journal Of Applied Meteorology*, 42(9), 1273-1284. doi: 10.1175/1520- 0450(2003)042<1273:pacoau>2.0.co;2

Earl, N., Simmonds, I., and Tapper, N. (2016). Weekly Cycles in Peak Time Temperatures and Urban Heat Island Intensity. *Environmental Research Letters*, 11(7), 074003. https://doi.org/10.1088/1748-9326/11/7/074003.eID/13592/Digital-Number-Radiance -and-Reflectance.aspx [Accessed 1 Mar. 2019].

El Kenawy, A. M., Lopez-Moreno, J. I., McCabe, M. F., Domínguez-Castro, F., Peña-Angulo, D., Gaber, I. M., ... Vicente-Serrano, S. M. (2021). The Impact of COVID-19 Lockdowns on Surface Urban Heat Island Changes and Air-Quality Improvements across 21 Major Cities in the Middle East.

Ellena, M., J. Ballester, P. Mercogliano, E. Ferracin, G. Barbato, G. Costa, and V. Ingole (2020). Social Inequalities in Heat-Attributable Mortality in the City of Turin, Northwest of Italy: A Time Series Analysis from 1982 to 2018. *Environ Health* 19.1, p. 116. doi: 10.1186/s12940-020-00667-x.

Fan, H., and Sailor, D. (2005). Modeling the Impacts of Anthropogenic Heating on the Urban Climate of Philadelphia: A Comparison of Implementations in Two PBL Schemes. *Atmospheric Environment*, 39(1), 73–84. https://doi.org/10.1016/j.atmosenv.2004.09.031.

Feng, H., Zhao, X., Chen, F., and Wu, L. (2014). Using land use change trajectories to quantify the effects of urbanization on urban heat island. *Advances In Space Research*, 53(3), 463-473. doi: 10.1016/j.asr.2013.11.028

Feng, R., Wang, F., Wang, K., Wang, H., and Li, L. (2021). Urban Ecological Land and Natural-Anthropogenic Environment Interactively Drive Surface Urban Heat Island: An Urban Agglomeration-Level Study in China. *Environment International*, 157, 106857. https://doi.org/10.1016/j.envint.2021.106857.

Feng, Z., Wang, X., Yuan, J., Zhang, Y., and Yu, M. (2023). Changes in Air Pollution, Land Surface Temperature, and Urban Heat Islands during the COVID-19 Lockdown in Three Chinese Urban Agglomerations. *Science of The Total Environment*, 892, 164496. https://doi.org/10.1016/j.scitotenv.2023.164496.

Fennessy, M. J., and Kinter, J. L. (2011). Climatic feedbacks during the 2003 European Heat Wave. *Journal of Climate*, 24(23), 5953–5967. doi:10.1175/2011jcli3523.1

Firozjaei, M. K., Weng, Q., Zhao, C., Kiavarz, M., Lu, L., and Alavipanah, S. K. (2020). Surface Anthropogenic Heat Islands in Six Megacities: An Assessment Based on a Triple-Source Surface Energy Balance Model. *Remote Sensing of Environment*, 242, 111751. https://doi.org/10.1016/j.rse.2020.111751.

Fouillet, a., Rey, G., Laurent, F., Pavillon, G., Bellec, S., Guihenneuc-Jouyaux, C., Hémon, D. (2006). Excess mortality related to the August 2003 heat wave in France. International *Archives of Occupational and Environmental Health*, 80(1), 16–24.

Gabriel, K. M. A., and Endlicher, W. R. (2011). Urban and rural mortality rates during heat waves in Berlin and Brandenburg, Germany. *Environmental Pollution*, 159(8–9), 2044–2050. doi:10.1016/j.envpol.2011.01.016

García, D. H. (2021a). Analysis of urban heat island and heat waves using sentinel-3 images: A study of Andalusian cities in Spain. *Earth Systems and Environment*, 6(1), 199–219. doi:10.1007/s41748-021-00268-9

Gartland, L. (2011). Heat islands: understanding and mitigating heat in urban areas, Routledge. *Atmospheric Environment*, (7), 769–779.

Gasparrini, A., B. Armstrong, and M. G. Kenward (2010). Distributed Lag NonLinear Models. *Statist. Med.* 29.21, pp. 2224–2234. doi: 10.1002/sim.3940.

Gasparrini, A. (n.d.). Distributed Lag Linear and Non-Linear Models: The R the Package Dlnm (), p. 17

Giannini, M., Belfiore, O., Parente, C. and Santamaria, R. (2015). Land Surface Temperature from Landsat 5 TM images: comparison of different methods using airborne thermal data. *Journal of Engineering Science and Technology Review*, 8(3), pp.83-90

Glocke, P., Bechtel, B., and Sismanidis, P. (2023). Consideration of Altered Anthropogenic Behavior during the First Lockdown and Its Effects on Air Pollutants and Land Surface Temperature in European Cities. *Atmosphere*, 14(6), 1025. https://doi.org/10.3390/atmos14061025.

Gosling, S.N., Lowe, J.A., McGregor, G.R. et al. Associations between elevated atmospheric temperature and human mortality: a critical review of the literature. *Climatic Change,* 92, 299–341 (2009). https://doi.org/10.1007/s10584-008-9441-x

Green, H., Bailey, J., Schwarz, L., Vanos, J., Ebi, K., and Benmarhnia, T. (2019). Impact of heat on mortality and morbidity in low and middle income countries: A review of the epidemiological evidence and considerations for future research. *Environmental Research*, 171, 80–91. doi:10.1016/j.envres.2019.01.010

Gronlund, C. J., Zanobetti, A., Wellenius, G. A., Schwartz, J. D., and O'Neill, M. S. (2016). Vulnerability to renal, heat and respiratory hospitalizations during extreme heat among U.S. elderly. *Climatic Change*, 136(3–4), 631–645. doi:10.1007/s10584-016-1638-9

Hamdi, R., Tronquo, E., Bogaerts, E., Hoang, K.-M., Loudeche, C., Claeys, E., Caluwaerts, S., Duchêne, F., Van Schaeybroeck, B., and Termonia, P. (2022). The Impact of COVID-19 Confinement Measures on the Canopy Urban Heat Island Intensity of Ghent (Belgium). https://doi.org/10.5194/egusphere-egu22-7193.

Hamilton, I. G., Davies, M., Steadman, P., Stone, A., Ridley, I., and Evans, S. (2009). The Significance of the Anthropogenic Heat Emissions of London's Buildings: A Comparison

against Captured Shortwave Solar Radiation. *Building and Environment*, 44(4), 807–817. https://doi.org/10.1016/j.buildenv.2008.05.024.

Harris Geospatial Solutions. (2017). Digital Number, Radiance, and Reflectance.[online]Available at http://www.harrisgeospatial.com/Home/NewsUpdates/TabId/170/ArtMID/735/Articl

Hashem A., Ryan B., Tony B.L, David C., Maury E., Gordon H., Hitcock D., Greg M., Tim O., Danny P., Alan P., Joyce R., David S. J., Haider T., James V., Darrell W., Katywh., B. 2013. Reducing Urban Heat Islands: Compendium of Strategies Urban Heat Island Basics. In: PROGRAMS, C. P. P. D. I. T. U. S. E. P. A. S. O. O. A. (ed.).

Heat Islands | US EPA. (2018). Retrieved from https://www.epa.gov/heat-island

Heaviside, C., Vardoulakis, S., and Cai, X.-M. (2016). Attribution of mortality to the urban heat island during heatwaves in the West Midlands, UK. *Environmental Health*, 15(S1). doi:10.1186/s12940-016-0100-9

Herbel, I., Croitoru, A.-E., Rus, A. V., Roşca, C. F., Harpa, G. V., Ciupertea, A.-F., and Rus, I. (2017). The impact of heat waves on surface urban heat island and local economy in Cluj-Napoca City, Romania. *Theoretical and Applied Climatology*, 133(3–4), 681–695. doi:10.1007/s00704-017-2196-4

How Cell Statistics works—Help | ArcGIS for Desktop. (2019). Retrieved 16 November 2019, from http://desktop.arcgis.com/en/arcmap/10.3/tools/spatial-analyst-toolbox/how-cell-statistics-works.htm#ESRI_SECTION1_1D1C9509B955465EA3F74C4C0B308A89

http://www.epa.gov/heatisland/resources/compendium.htm.

https://www.usgs.gov/media/files/landsat-8-data-users-handbook (Accessed 19 Jun. 2019).

Ichinose, F. Matsumoto, K. Kataoka (2008). Chapter 15-Counteracting Urban Heat Islands in Japan P. Droege (Ed.), *Urban Energy Transition*, Elsevier, Amsterdam, pp. 365-380

ISO 10551. (1995). Ergonomics of the thermal environment - Assessment of the influence of the thermal environment using subjective judgment scales. Genève.

Jacobson, J., and Forsyth, A. (2008). Seven American TODs: Good Practices for Urban Design in Transit-Oriented Development Projects. *Journal of Transport and Land Use*, 1(2). https://doi.org/10.5198/jtlu.v1i2.67.

Jandaghian, Z., and Akbari, H. (2018). The effects of increasing surface reflectivity on heat-related mortality in Greater Montreal area, Canada. *Urban Climate*, 25, 135–151. doi:10.1016/j.uclim.2018.06.002

Jenks, George F. (1967) The Data Model Concept in Statistical Mapping, *International Yearbook of Cartography,* 7: 186-190.

Jin, K., Wang, F., and Wang, S. (2020). Assessing the Spatiotemporal Variation in Anthropogenic Heat and Its Impact on the Surface Thermal Environment over Global Land Areas. *Sustainable Cities and Society*, 63, 102488. https://doi.org/10.1016/j.scs.2020.102488.

Keikhosravi, Q. (2019). The effect of heat waves on the intensification of the Heat Island of Iran's metropolises (Tehran, Mashhad, Tabriz, Ahvaz). *Urban Climate*, 28, 100453. https://doi.org/10.1016/j.uclim.2019.100453.

Kei Wang Cheung, H. (2011). An urban heat island study for building and urban design (Doctoral). University of Manchester.

Kottek, M., Grieser, J., Beck, C., Rudolf, B., and Rubel, F. (2006). World Map of the Köppen-Geiger Climate Classification Updated. *Meteorologische Zeitschrift*, 15(3), 259–263. https://doi.org/10.1127/0941-2948/2006/0130.

Kumari, P., and Toshniwal, D. (2020). Impact of Lockdown on Air Quality over Major Cities across the Globe during COVID-19 Pandemic. *Urban Climate*, 34, 100719. https://doi.org/10.1016/j.uclim.2020.100719.

Landsat 8 Data Users Handbook. [online] Available at:

Lee, S.-H., McKeen, S. A., and Sailor, D. J. (2014). A Regression Approach for Estimation of Anthropogenic Heat Flux Based on a Bottom-up Air Pollutant Emission Database. *Atmospheric Environment*, 95, 629–633. https://doi.org/10.1016/j.atmosenv.2014.07.009.

Lee, X. (2017). Energy Balance, Evaporation, and Surface Temperature. *Springer Atmospheric Sciences*, 191–213. https://doi.org/10.1007/978-3-319-60853-2_10.

Letiště Praha. Available at: https://www.prg.aero/letiste-praha-odbavilo-za-lonsky-rok-temer-3-7-milionu-cestujicich (accessed February 4, 2023).

Lhotka, O., Kyselý, J., and Farda, A. (2017). Climate change scenarios of heat waves in Central Europe and their uncertainties. *Theoretical and Applied Climatology*, 131(3–4), 1043–1054. https://doi.org/10.1007/s00704-016-2031-3

Li, D., Sun, T., Liu, M., Wang, L., and Gao, Z. (2016). Changes in wind speed under heat waves enhance urban heat islands in the Beijing Metropolitan Area. *Journal of Applied Meteorology and Climatology*, 55(11), 2369–2375. doi:10.1175/jamc-d-16-0102.1

Li, D., Sun, T., Liu, M., Yang, L., Wang, L., and Gao, Z. (2015). Contrasting responses of urban and rural surface energy budgets to heat waves explain synergies between urban

heat islands and heat waves. *Environmental Research Letters*, 10(5), 054009. doi:10.1088/1748-9326/10/5/054009

Lin, Y., Jim, C., Deng, J., and Wang, Z. (2018). Urbanization effect on spatiotemporal thermal patterns and changes in Hangzhou (China). *Building And Environment*, 145, 166-176. doi: 10.1016/j.buildenv.2018.09.020

Lindberg, F., Grimmond, C. S. B., Yogeswaran, N., Kotthaus, S., and Allen, L. (2013). Impact of City Changes and Weather on Anthropogenic Heat Flux in Europe 1995–2015. *Urban Climate*, 4, 1–15. https://doi.org/10.1016/j.uclim.2013.03.002.

Liu, F., Wang, M., and Zheng, M. (2021). Effects of COVID-19 Lockdown on Global Air Quality and Health. *Science of The Total Environment*, 755, 142533. https://doi.org/10.1016/j.scitotenv.2020.142533.

Liu, Z., Lai, J., Zhan, W., Bechtel, B., Voogt, J., Quan, J., ... Li, J. (2022). Urban Heat Islands

Significantly Reduced by COVID‐19 Lockdown. *Geophysical Research Letters*, 49(2). https://doi.org/10.1029/2021gl096842.

LP DAAC - MCD19A2. Available at: https://lpdaac.usgs.gov/products/mcd19a2v006/ (accessed January 3, 2023).

Magli, S., Lodi, C., Lombroso, L., Muscio, A., and Teggi, S. (2014). Analysis of the urban heat island effects on building energy consumption. *International Journal Of Energy And Environmental Engineering*, 6(1), 91-99. doi: 10.1007/s40095-014-0154-9

Majkowska, A., Kolendowicz, L., Półrolniczak, M., Hauke, J., and Czernecki, B. (2016). The urban heat island in the city of Poznań as derived from Landsat 5 TM. *Theoretical And Applied Climatology*, 128(3-4), 769-783. doi: 10.1007/s00704-016-1737-6

Mazhar, U., Jin, S., Bilal, M., Arfan Ali, Md., and Khan, R. (2021). Reduction of Surface Radiative Forcing Observed from Remote Sensing Data during Global COVID-19 Lockdown. *Atmospheric Research*, 261, 105729.

Meng, Q., Qian, J., Schlink, U., Zhang, L., Hu, X., Gao, J., and Wang, Q. (2023). Anthropogenic Heat Variation during the COVID-19 Pandemic Control Measures in Four Chinese Megacities. *Remote Sensing of Environment*, 293, 113602. https://doi.org/10.1016/j.rse.2023.113602.

Menut, L., Flamant, C., Pelon, J., and Flamant, P. (1999). Urban boundary-layer height determination from lidar measurements over the Paris area. *Applied Optics*, 38(6), 945. doi: 10.1364/ao.38.000945

Mijani, N., Karimi Firozjaei, M., Mijani, M., Khodabakhshi, A., Qureshi, S., ... Alavipanah, S. K. (2023). Exploring the Effect of COVID-19 Pandemic Lockdowns on Urban Cooling: A Tale of Three Cities. *Advances in Space Research*, 71(1), 1017–1033. https://doi.org/10.1016/j.asr.2022.09.052.

Muhammad, S., Long, X., and Salman, M. (2020). COVID-19 Pandemic and Environmental Pollution: A Blessing in Disguise? *Science of The Total Environment*, 728. https://doi.org/10.1016/j.scitotenv.2020.138820.

(N.d.). Retrieved from https://geoportalpraha.cz/en

Obyvatelstvo. Available at: https://www.czso.cz/csu/xa/obyvatelstvo-xa (accessed December 20, 2023).

Oke, T. (1973). City size and the urban heat island. *Atmospheric Environment* (1967), 7(8), 769-779. doi: 10.1016/0004-6981(73)90140-6

Oke, T. (1976). The distinction between canopy and boundary-layer urban heat islands. *Atmosphere* 14(4), 268–277.

Oke, T. R., Mills, G., Christen, A., and Voogt, J. A. (2017). *Urban Climates*. Cambridge University Press.

Oke, T. R. (1982). The energetic basis of the urban heat island. Q. J. R. *Meteorol. Soc.* 108, 1–24.

Oke, T. R. (1987). *Boundary Layer Climates*. Psychology Press.

Oke, T. R. *Boundary Layer Climates*. Psychology Press, 1987.

Ouředníček, M. *Prague and Central Bohemia*. Charles University in Prague, Karolinum Press, 2022.

Our World in Data. COVID-19 Stringency Index. Available at: https://ourworldindata.org/covid-stringency-index (accessed January 20, 2023).

Pal, S., Das, P., Mandal, I., Sarda, R., Mahato, S., Nguyen, K.-A., ... Talukdar, S. (2021). Effects of Lockdown Due to COVID-19 Outbreak on Air Quality and Anthropogenic Heat in an Industrial Belt of India. *Journal of Cleaner Production*, 297, 126674. https://doi.org/10.1016/j.jclepro.2021.126674.

Parida, B. R., Bar, S., Kaskaoutis, D., Pandey, A. C., Polade, S. D., and Goswami, S. (2021). Impact of COVID-19 Induced Lockdown on Land Surface Temperature, Aerosol, and Urban Heat in Europe and North America. *Sustainable Cities and Society*, 75, 103336. https://doi.org/10.1016/j.scs.2021.103336.

Patiño, W. R., and Duong, V. M. (2021). Intercomparison of Gaussian Plume Dispersion Models Applied to Sulfur Dioxide Emissions from a Stationary Source in the Suburban Area of Prague, Czech Republic. *Environmental Modeling and Assessment*, 27(1), 119–137. https://doi.org/10.1007/s10666-021-09803-4.

Peng, J., Liu, Q., Wang, L., Liu, Q., Fan, W., Lu, M., and Wen, J. (2015). Characterizing the Pixel Footprint of Satellite Albedo Products Derived from MODIS Reflectance in the

Heihe River Basin, China. *Remote Sensing*, 7(6), 6886–6907. https://doi.org/10.3390/rs70606886.

Peng, J., Xie, P., Liu, Y., and Ma, J. (2016). Urban thermal environment dynamics and associated landscape pattern factors: A case study in the Beijing metropolitan region. *Remote Sensing Of Environment*, 173, 145-155. doi: 10.1016/j.rse.2015.11.027

Potter, C., and Alexander, O. (2021). Impacts of the San Francisco Bay Area Shelter-in-Place during the COVID-19 Pandemic on Urban Heat Fluxes. *Urban Climate*, 37, 100828. https://doi.org/10.1016/j.uclim.2021.100828.

Qian, J., Meng, Q., Zhang, L., Schlink, U., Hu, X., and Gao, J. (2023). Characteristics of Anthropogenic Heat with Different Modeling Ideas and Its Driving Effect on Urban Heat Islands in Seven Typical Chinese Cities. *Science of The Total Environment*, 886, 163989. https://doi.org/10.1016/j.scitotenv.2023.163989.

Raj, S., Paul, S. K., Chakraborty, A., and Kuttippurath, J. (2020). Anthropogenic Forcing Exacerbating the Urban Heat Islands in India. *Journal of Environmental Management*, 257, 110006. https://doi.org/10.1016/j.jenvman.2019.110006.

Raya, A. B., Hasibuan, H. S., and Sodri, A. (2022). Thermal Comfort-Based Spatial Planning Model in Jakarta Transit-Oriented Development (TOD). *Atmosphere*, 13(4), 565. https://doi.org/10.3390/atmos13040565.

Revathy, S. M., Rangaraj, A. G., Srinath, Y., Boopathi, K., Shobana Devi, A., Balaraman, K., and Prasad, D. M. R. (2021). Impact on Solar Radiation Parameters in India during COVID-19 Lockdown: A Case Study. *International Journal of Sustainable Energy*, 40(8), 806–820. https://doi.org/10.1080/14786451.2021.1893726.

Rizwan, A., Dennis, L., and Liu, C. (2008). A review on the generation, determination and mitigation of Urban Heat Island. *Journal Of Environmental Sciences*, 20(1), 120-128. doi: 10.1016/s1001-0742(08)60019-4

Ročenka dopravy Praha 2020. Available at: https://www.tsk-praha.cz/static/udi-rocenka-2020-cz.pdf (accessed March 20, 2023).

Roshan, G., Sarli, R., and Grab, S. W. (2021). The Case of Tehran's Urban Heat Island, Iran: Impacts of Urban 'Lockdown' Associated with the COVID-19 Pandemic. *Sustainable Cities and Society*, 75, 103263. https://doi.org/10.1016/j.scs.2021.103263.

Safarrad, T., Ghadami, M., and Dittmann, A. (2022). Effects of COVID-19 Restriction Policies on Urban Heat Islands in Some European Cities: Berlin, London, Paris, Madrid, and Frankfurt. *International Journal of Environmental Research and Public Health*, 19(11), 6579. https://doi.org/10.3390/ijerph19116579.

Sahani, N., Goswami, S. K., and Saha, A. (2020). The Impact of COVID-19 Induced Lockdown on the Changes of Air Quality and Land Surface Temperature in Kolkata City,

India. *Spatial Information Research*, 29(4), 519–534. https://doi.org/10.1007/s41324-020-00372-4.

Sailor, D. J., and Lu, L. (2004). A top-down methodology for developing diurnal and seasonal anthropogenic heating profiles for urban areas. *Atmospheric Environment*, 38(17), 2737– 2748.

Santamouris, M. (2020). Recent progress on urban overheating and Heat Island Research. integrated assessment of the energy, environmental, vulnerability and health impact. Synergies with the global climate change. *Energy and Buildings*, 207, 109482. doi:10.1016/j.enbuild.2019.109482

Scheifinger, H., Menzel, A., Koch, E., Peter, C., and Ahas, R. (2002). Atmospheric Mechanisms Governing the Spatial and Temporal Variability of Phenological Phases in Central Europe. *International Journal of Climatology*, 22(14), 1739–1755. https://doi.org/10.1002/joc.817.

Sentinel-5P OFFL NO2: Offline Nitrogen Dioxide. Available at: https://developers.google.com/earth-engine/datasets/catalog/COPERNICUS_S5P_OFFL_L3_NO2#description (accessed January 20, 2023).

Sheridan, S. C., and Dixon, P. G. (2017). Spatiotemporal trends in human vulnerability and adaptation to heat across the United States. Anthropocene, 20, 61–73. https://doi.org/10.1016/j.ancene.2016.10.001

Simulated historical climate and weather data for Prague. Available at: https://www.meteoblue.com/en/weather/historyclimate/climatemodelled/prague_czechia_3067696 (accessed March 17, 2023).

Sismanidis, P., Bechtel, B., Keramitsoglou, I., Liu, Z., and Zhan, W. (2023). The Intensity of Surface Urban Heat Islands in the Global North during the COVID-19 Lockdowns. *2023 Joint Urban Remote Sensing Event (JURSE)*. https://doi.org/10.1109/jurse57346.2023.10144159.

Smargiassi, A., Goldberg, M. S., Plante, C., Fournier, M., Baudouin, Y., and Kosatsky, T. (2009). Variation of daily warm season mortality as a function of micro-urban heat islands. *Journal of Epidemiology and Community Health*, 63(8), 659–664. https://doi.org/10.1136/jech.2008.078147

Statistics VDB. (2019). Retrieved 15 November 2019, from https://vdb.czso.cz/vdbvo2/faces/en/index.jsf?page=statistikyandkatalog=30845

Stewart, I., and Oke, T. (2012). Local Climate Zones for Urban Temperature Studies. *Bulletin Of The American Meteorological Society*, 93(12), 1879-1900. doi: 10.1175/bams-d-11-00019.1

Stone, B., Vargo, J., Liu, P., Habeeb, D., DeLucia, A., Trail, M., . . . Russell, A. (2014). Avoided Heat-Related Mortality through Climate Adaptation Strategies in Three US Cities. *PLoS ONE*, 9(6), e100852. https://doi.org/10.1371/journal.pone.0100852

Tobler, W. R. (1970). A Computer Movie Simulating Urban Growth in the Detroit Region. E*conomic Geography*, 46, 234. https://doi.org/10.2307/143141.

Venter, Z. S., Aunan, K., Chowdhury, S., and Lelieveld, J. (2020). COVID-19 Lockdowns Cause Global Air Pollution Declines. *Proceedings of the National Academy of Sciences*, 117(32), 18984–18990. https://doi.org/10.1073/pnas.2006853117.

Vicedo-Cabrera, A. M., Scovronick, N., Sera, F., Royé, D., Schneider, R., Tobias, A., . . . Gasparrini, A. (2021). The burden of heat-related mortality attributable to recent human-induced climate change. *Nature Climate Change*, 11(6), 492–500. https://doi.org/10.1038/s41558-021-01058-x

Voogt, J. (2007). How Researchers Measure Urban Heat Islands. *United States Environmental Protection Agency (EPA)*, State and Local Climate and Energy Program, Heat Island Effect, Urban Heat Island Webcasts and Conference Calls.

Wan, Z. MODIS Land Surface Temperature Products Users' Guide. https://lpdaac.usgs.gov/documents/447/MOD11_User_Guide_V4.pdf (accessed 2023 -01 -11).

Wang, W., and He, B.-J. (2023). Co-Occurrence of Urban Heat and the COVID-19: Impacts, Drivers, Methods, and Implications for the Post-Pandemic Era. *Sustainable Cities and Society*, 90, 104387. https://doi.org/10.1016/j.scs.2022.104387.

Watson, C. (2012). *Analysis of Urban Heat Island Climates along the I-85/I-40 Corridor in Central North Carolina* (Ph.D.). University of North Carolina.

Wawer, Rafal & Nowocien, Eugeniusz & Łopatka, Artur. (2016). An Approach To Dynamic Trafficability Mapping As A Component Of Battle Management Systems. *Estonian Journal of Military Studies*. ENDC Proceedings 21. 48-57.

Weng, Q., Liu, H., Liang, B., and Dengsheng Lu, D. (2008). The Spatial Variations of Urban Land Surface Temperatures: Pertinent Factors, Zoning Effect, and Seasonal Variability. *IEEE Journal Of Selected Topics In Applied Earth Observations And Remote Sensing*, 1(2), 154-166. doi: 10.1109/jstars.2008.917869

Wey, W.-M. (2015). Smart Growth and Transit-Oriented Development Planning in Site Selection for a New Metro Transit Station in Taipei, Taiwan. *Habitat International*, 47, 158–168. https://doi.org/10.1016/j.habitatint.2015.01.020.

Whitman, S., Good, G., Donoghue, E. R., Benbow, N., Shou, W., and Mou, S. (1997). Mortality in Chicago attributed to the July 1995 heat wave. *American Journal of Public Health*, 87(9), 1515–1518.

Wu, X., Zhang, L., and Zang, S. (2019). Examining seasonal effect of urban heat island in a coastal city. *PLOS ONE*, 14(6), e0217850. doi: 10.1371/journal.pone.0217850

Yang, L., Qian, F., Song, D., and Zheng, K. (2016). Research on Urban Heat-Island Effect. *Procedia Engineering*, 169, 11-18. doi: 10.1016/j.proeng.2016.10.002

Zakšek, K., and Oštir, K. (2012). Downscaling land surface temperature for urban heat island diurnal cycle analysis. *Remote Sensing of Environment*, 117, 114–124. https://doi.org/10.1016/j.rse.2011.05.027

Zhang, H., Qi, Z., Ye, X., Cai, Y., Ma, W. and Chen, M. (2013). Analysis of land use/land cover change, population shift, and their effects on spatiotemporal patterns of urban heat islands in metropolitan Shanghai, China. *Applied Geography*, 44, pp.121-133.

Zhang, J., Wu, L., Yuan, F., Dou, J., and Miao, S. (2015). Mass Human Migration and Beijing's Urban Heat Island during the Chinese New Year Holiday. *Science Bulletin*, 60(11), 1038–1041. https://doi.org/10.1007/s11434-015-0809-9.

Zhang, X., Zhong, T., Feng, X., and Wang, K. (2009). Estimation of the relationship between vegetation patches and urban land surface temperature with remote sensing. *International Journal Of Remote Sensing*, 30(8), 2105-2118. doi: 10.1080/01431160802549252

Zhou, D., Xiao, J., Bonafoni, S., Berger, C., Deilami, K., and Zhou, Y. et al. (2018). Satellite Remote Sensing of Surface Urban Heat Islands: Progress, Challenges, and Perspectives. *Remote Sensing*, 11(1), 48. doi: 10.3390/rs11010048

Zhou, D., Zhao, S., Liu, S., Zhang, L., and Zhu, C. (2014). Surface Urban Heat Island in China's 32 Major Cities: Spatial Patterns and Drivers. *Remote Sensing of Environment*, 152, 51–61. https://doi.org/10.1016/j.rse.2014.05.017.

Chapter VII

Curriculum Vitae

& List of Publications

Personal

Tugba Dogan

Websites: orcid.org/my-orcid?orcid=0000-0002-6854-8959
                   researchgate.net/profile/Tugba-Dogan-10
Email: dogan@fzp.czu.cz

Education

Czech University of Life Sciences Prague, CZ
P.hD., Environmental Modeling   expected to finish in 2024

Ondokuz Mayıs University   Samsun, TR
Master, Geomatics Engineering   2021

Czech University of Life Sciences Prague, CZ
Master, Landscape Planning   2017

Ondokuz Mayıs University Samsun, TR
Bachelor, Geomatics Engineering   2015

Internship

Turkish State Meteorological Service Ankara, TR
Regional climate models   July - September 2018

University of Ljubljana Ljubljana, SI
Surface urban heat islands   July -September 2017

Czech Technical University   Prague, CZ
Remote sensing practices   August -September 2015

Devran Surveying Company Ankara, TR
Digitization of Expropriation Plans   July-September 2014

General Directorate of State Hydraulic Works Ankara, TR
Evaluation of areas to be expropriated using GIS   July -September 2012

Workshops

2023. "Training of urban micrometeorological data end-users" FAIRNESS Summer school 2023, Ghent, BE.

2022. "From Climate Projections to Climate Impacts via Regional Downscaling" IS-ENES3 Central and Eastern Europe Autumn Schools", Prague, CZ.

Conference

DOGAN, T.; URBAN, A., The effect of the COVID-19 lockdown on the surface urban heat island in Prague, Czech Republic. (2023), 23rd International Congress of Biometeorology, Tempe, Arizona, USA

DOGAN, T.; URBAN, A., Links between the spatial distribution of the

surface urban heat island and heat-related mortality in Prague, Czech Republic. (2022), EGU General Assembly 2022, Vienna, AT.

DOGAN, T.; HANEL, M., An Analysis of the COVID-19 Lockdown Impact on the Urban Heat Island Effect Using Satellite Images. (2020), Climatological, Meteorological, and Environmental factors in the COVID-19 pandemic, World Meteorological Organization, Online.

DOGAN, T.; OZTURK, D., Spatiotemporal Analysis of The Urban Heat Island Effect, A Case Study in Samsun, Turkey. (2019), Hydrology, GIS and environment, Prague, CZ.

DOGAN, T.; KREVS, M., Impacts of Land Use Land Cover Changes on Urban Heat Island in Ljubljana, Slovenia. (2018), Hydrology, GIS and environment, Prague, CZ.

DOGAN, T.; HANEL, M., Effects of Land Cover Changes on Surface Urban Heat Island (SUHI) Using CORINE Land Cover Change (CLC) Products: The Case of Prague. (2018), Kostelecké inspirování 2018, CZ.

Publication

Accepted & Published:

DOGAN, T.; URBAN, A.; HANEL, M., Effect of COVID-19 Lockdown on Urban Heat Island Dynamics in Prague, Czechia. Remote Sensing. 16 (2024), x. https://doi.org/10.3390/xxxxx

DOGAN, T.; HANEL, M.; OGUZ, K., AND DEMIRCAN, M., Assessment of the Urban Heat Island Effect Under Current and Climate Change Conditions in Istanbul. International Multidisciplinary Scientific GeoConference EXPO Proceedings, 19 (2019), 891–898. https://doi.org/10.5593/sgem2019/4.1/s19.113

In preparation:

DOGAN, T., HANEL, M., Evaluating the effects of land cover change on the change of surface urban heat island.

DOGAN, T., URBAN, A., Links between the spatial distribution of the land surface temperature and heat-related mortality in Prague, Czech Republic.

Teaching

Teaching assistant at the Czech University of Life Sciences for the following courses: Spatial Planning, Air Pollution, and Land Management.

Supervision

Greenway design in an urban environment: tree placement
Valtteri Paananen, 2021